Islamic University of Technology

Board Bazar, Gazipur-1704, Bangladesh.

Highly Sensitive Plasmonic Nano Sensor for Lab On a Chip Application

by

A. K. M. Rakib 180021104

Ahnaf Tahmid Bin Siddique 180021130

Mohd. Abu Bakar Siddique 180021139

Md. Raisul Muttaqi 180021234

in Consideration of Partial Fulfillment for the Requirements of the Degree of

BACHELOR OF SCIENCE

IN

ELECTRICAL AND ELECTRONIC ENGINEERING

Department of Electrical and Electronic Engineering

May, 2023

Highly Sensitive Plasmonic Nano Sensor for Lab On a Chip Application

Submitted by

A. K. M. Rakib 180021104
Ahnaf Tahmid Bin Siddique 180021130
Mohd. Abu Bakar Siddique 180021139
Md. Raisul Muttaqi 180021234

has been approved on 4^{th} June, 2023

Dr. Rakibul Hasan Sagor
Professor and Supervisor
Department of Electrical and Electronic Engineering
Islamic University of Technology

Declaration of Authorship

This is to certify that the work presented in this Thesis entitled, “Highly sensitive plasmonic nano sensor for lab on a chip application”, is the outcome of the research carried out under the supervision of Dr. Rakibul Hasan Sagor, Professor, Islamic University of Technology.

Signatures of the Candidates

A. K. M. Rakib

Ahnaf Tahmid Bin Siddique

Mohd. Abu Bakar Siddique

Md. Raisul Muttaqi

Acknowledgement

Throughout the duration of our thesis, Dr. Sagor has provided us with unwavering support and invaluable guidance. His insight, knowledge, and perseverance were crucial to the success of our work. His mentoring has not only contributed to the success of this endeavor, but also to our own learning and development. Additionally, we would like to express our gratitude to the faculty, personnel, and fellow students at the Islamic University of Technology (IUT). Their consistent support, helpful feedback, and encouragement have fostered an environment that is conducive to learning and research. This endeavor could not have been completed without IUT's facilities, resources, and community of support. Our time at IUT and Dr. sagor's guidance have been indispensable to our growth as scholars and professionals, and we are profoundly grateful for their contributions to our voyage.

Contents

List of Figures

List of Tables

List of Abbreviations

EM	Electromagnetic
EOT	Extraordinary Optical Transmission
FEM	Finite Element Method
FOM	Figure of Merit
LSPR	Localized Surface Plasmon Resonance
MIM	Metal-Insulator-Metal
MIR	Mid-Infrared
NIR	Near Infrared
NP	Nanoparticles
Q-factor	Quality factor
RI	Refractive Index
RIU	Refractive Index Unit
SPP	Surface Plasmon Polariton
SPR	Surface Plasmon Resonance
TM	Transverse Magnetic
VIS	Visible Light

Abstract

Numerous studies have used the Drude model to optimize silver-based Metal-Insulator-Metal plasmonic sensors for some limited sensing applications; however, Lab-on-a-chip sensing for cell protein concentration measurement still needs to be accomplished. Furthermore, little study has been conducted on sensing for the salinity measurement of seawater, Bovine serum albumin concentration measurement, human tissue categorization, mitigating the oxidation issue of these sensors, and nanofabrication challenges. In this article, a Metal-Insulator-Metal based oxidation free material (gold modeled with Drude-Lorentz model) built round-edged hexagonal plasmonic refractive index sensor with nanorods embedded both in the straight waveguide and resonator has been investigated using the Finite element method (FEM) for all of the above sensing applications. This sensor achieves 19.05nm/g/100mL and 1476.6 nm/ppm sensitivity for cell protein concentration and salinity measurement. The sensor's max sensitivity and Sensing Resolution are 9231.7 nm /RIU and $1.083 * 10^{-7}$. This sensor has also been employed as an electromagnetic interference-free temperature sensor using toluene, achieving 5.16 nm/°C sensitivity. Thus, this label-free and low-footprint sensor can be employed to study the salinity of seawater, which is linked with global warming and the earth's hydrologic cycle, study protein concentration for nanomedicine applications, and Lab-on-chip sensing as an oxidation-free alternative to silver-based sensors.

Chapter 1

Introduction

Nanophotonics is the science and engineering of light-matter interaction at the sub-wavelength scale with an objective of minimizing the optical devices while keeping its high frequency properties. The dimension of traditional semiconductor devices like MOSFETs can be miniaturized into the deep submicron range which enables high density integration on a chip. But the speed of those devices are limited to a few GHz. On the other hand, optical devices have very high operating speeds, but their size can not be reduced easily because of the diffraction limit of light which impedes the localization of electromagnetic waves into regions that are smaller than the operating wavelength. Therefore, nanophotonics attempts to overcome the restrictions posed by diffraction limit by exploiting the properties of light-matter interaction and achieve both high operating speed and miniatured size. One of the branches of nanopho-

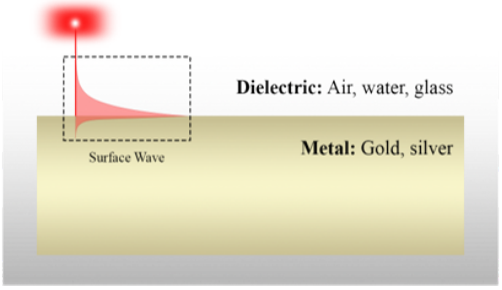

Figure 1.1: Structure for SPP propagation at a single interface between a metal and a dielectric

tonics is plasmonics which deals with generating, manipulating and detecting electromagnetic waves at optical frequency beyond the diffraction limit. Plasmon is a quasiparticle which arises from the coupling of the incident photon and coherently oscillating electrons which are present in the material. When plasmon propagates along the interface of metal and dielectric it is called surface plasmon polariton (SPP). SPP is a guided electromagnetic wave that propagates along the surface of a metal and dielectric interface while decaying

evanescently [28] which is illustrated in fig 1.1. As metal and dielectric have permittivity of opposite signs below the plasma frequency, it enables the generation and propagation of SPP [29] along the interface between them. This enables the construction of different plasmonic structures like directional couplers [30], reflectors [31], logic gates [32], Splitters [2], absorbers [3], demultiplexers [33], and Refractive index (RI) sensors [34–37].

1.1 Plasmonic logic gates

Plasmonic logic gates represent an intriguing intersection of nanotechnology, optics, and computing, offering a new method of information processing that has the potential to revolutionize the speed and efficiency of future computing technologies. Traditional logic gates, the fundamental building blocks of digital circuits, execute Boolean algebra operations such as AND, OR, and NOT using electronic signals. In contrast, plasmonic logic gates utilize surface plasmon polaritons (SPPs) to control and manipulate light on a nanoscale scale. These

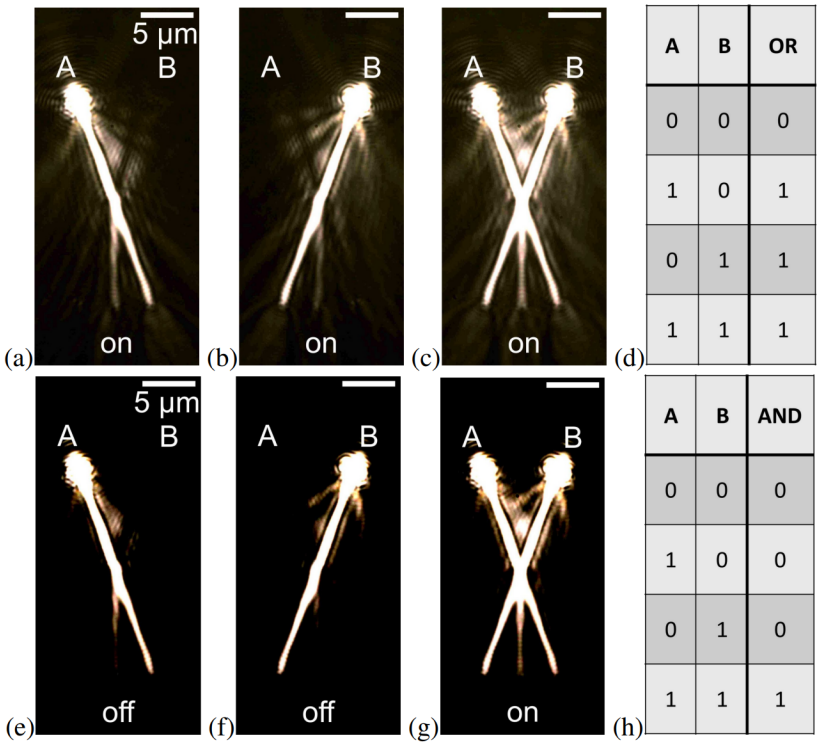

A	B	OR
0	0	0
1	0	1
0	1	1
1	1	1

A	B	AND
0	0	0
1	0	0
0	1	0
1	1	1

Figure 1.2: Schematic of an experimental realization of logic gates by Birr et al. [1].

plasmonic logic gates perform logical operations using light rather than electrical currents. By manipulating the characteristics of the SPPs, such as phase and amplitude, these gates are able to process optical signals at incredibly high velocities, significantly quicker than their electronic counterparts. There are numerous potential applications for plasmonic logic circuits, especially in the fields of optical computing and telecommunication, where the speed and miniaturization made possible by plasmonics could lead to significant advancements.

Before plasmonic logic gates can be extensively used in real-world applications, however, a number of technical obstacles, such as signal loss and implementation difficulties, must be surmounted. As our understanding and control of plasmonics continue to advance, these microscopic light-manipulating structures may play a pivotal role in the future of information processing, ushering in the era of light-based computers and ultrafast optical communications. Birr et al. [1] experimentally realized logic gates and half-adder illastrated in fig 1.2.

1.2 Plasmonic Splitter

Plasmonic splitters, a fundamental component of nanophotonics, utilize the exceptional properties of surface plasmon polaritons (SPPs) to control and manipulate light at the nanoscale. These properties are utilized by plasmonic splitters to divide an incoming light signal into

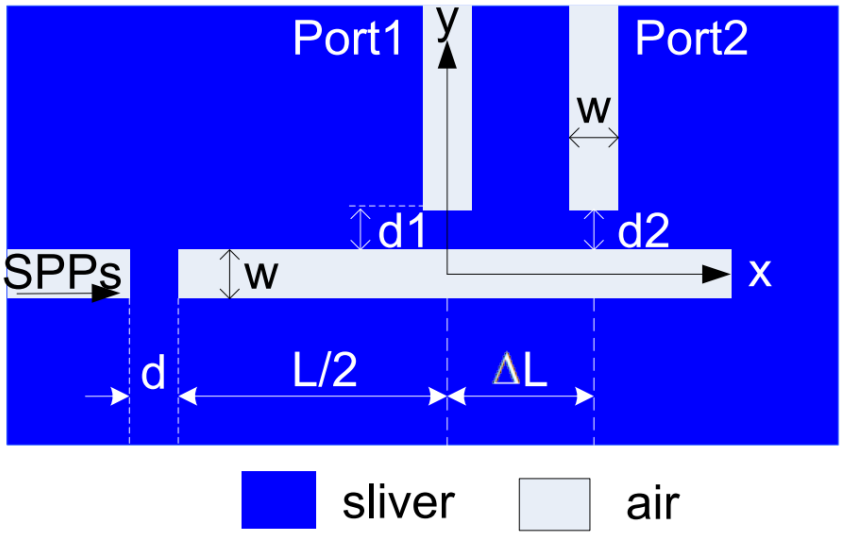

Figure 1.3: Schematic of a splitter system proposed by Guo et al. [2].

two or more output signals. They function by guiding light waves along the surface of a metal and then dividing those waves into separate paths, analogous to a traffic light for light. This technology possesses enormous potential, especially in the disciplines of integrated optics, optical communications, and biosensing. Nonetheless, substantial obstacles must be overcome before this potential can be fully realized. For instance, ongoing research and development focuses on the management of inherent loss, practical implementation, and ensuring stability under varying environmental conditions. Given the advancements in nanotechnology and photonics, plasmonic splitters continue to be an intriguing area of research with the potential to revolutionize a wide range of applications, including ultrafast computing and highly sensitive detection systems. One typical structure is presented in fig 1.3.

1.3 Plasmonic Absorbers

Plasmonic absorbers are a fascinating aspect of nanophotonics that utilize the unique properties of surface plasmon polaritons (SPPs) to absorb light on a nanoscale scale. A plasmonic absorber is designed to absorb light of a specific wavelength efficiently, making it a highly selective and effective instrument for light absorption and manipulation. These nanostructured devices have numerous potential applications, including solar energy harvesting, optical detection, and imaging. Plasmonic absorbers can potentially enhance the efficacy of solar cells by absorbing more sunlight and converting it into electrical energy. Due to their effective light absorption properties, these absorbers can enhance the sensitivity of thermal imaging and sensor systems. As with other cutting-edge technologies, the practical implementation of plasmonic absorbers faces obstacles, including the management of loss and the development of stable, reproducible nanoscale fabrication techniques. Despite these obstacles, plasmonic

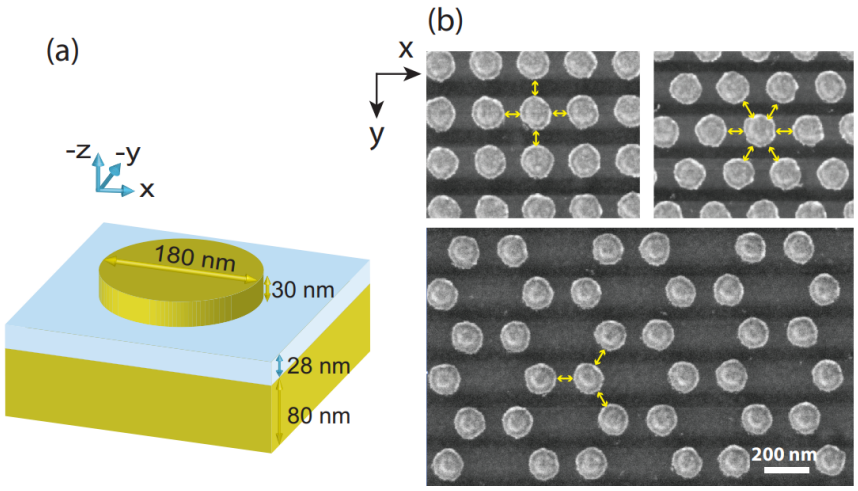

Figure 1.4: Schematic of an experimental metamaterial absorber with gold nanodisks proposed by by Chen et al. [3].

absorbers are an active area of research with the potential to have a significant impact on numerous industries and technologies due to their unique capabilities. As our understanding and control of light-matter interactions at the nanoscale continue to expand, we can anticipate that plasmonic absorbers will play a greater role in future optical technologies. An experimental plasmonic absorber is presented in fig 1.4

1.4 Plasmonic Filters

Plasmonic filters are one-of-a-kind optical devices that employ the principles of plasmonics to nanoscale light filtering. These devices have attracted considerable interest in the field of nanophotonics due to their ability to control and manipulate light beyond the diffraction

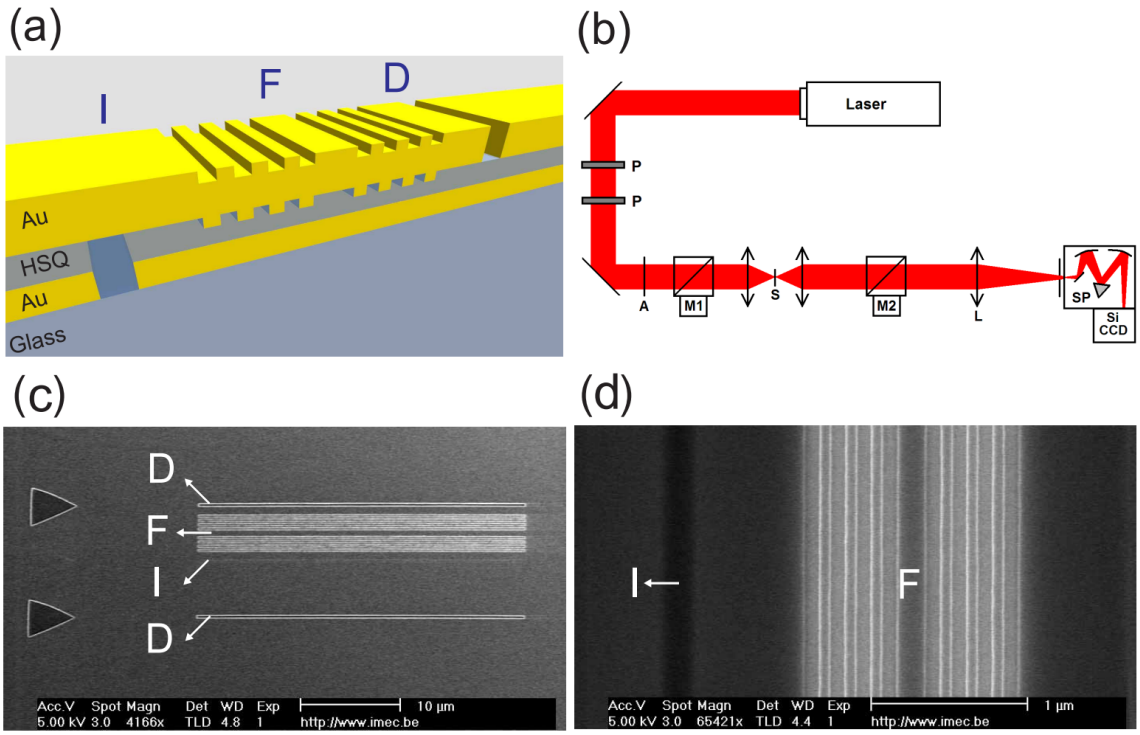

Figure 1.5: Experimental plasmonic filter construction by Neutens et al. [4]. (a) Diagrammatic depiction of the plasmonic crystal resonator integrated with a waveguide [4]. (b) Diagrammatic depiction of the transmission apparatus setup [4]. (c) Overhead view of a photograph taken by a scanning electron microscope showcasing a single plasmonic crystal filter. The locations for injection, detection, and the filter are labeled with the letters I, D, and F respectively [4]. (d) Closer examination of the filter area prior to the application of the top gold layer [4].

limit. Resonance conditions associated with plasmonic structures govern the operation of a plasmonic filter. When light interacts with these structures, only those wavelengths that correspond to the resonance conditions are absorbed or transmitted, while the rest are reflected. This allows the filter to selectively transmit or block specific wavelengths of light, much like conventional optical filters but on a much smaller scale. Plasmonic filters have a vast array of potential applications. They can be used to filter out disturbance and improve signal clarity in telecommunications. They can be used in imaging systems to selectively filter light for improved image acquisition. In addition, they can be utilized in biosensing to selectively detect light signals corresponding to various biological markers, providing a potent instrument for disease detection and monitoring. Despite the fact that plasmonic filters offer promising prospects, there are still several obstacles to their practical application. These include issues associated with nanoscale fabrication, managing energy loss associated with plasmonic structures, and ensuring the filter's performance is consistent and reliable. As research advances and solutions to these obstacles are discovered, plasmonic filters are expected to make significant contributions to a variety of applications in optics and photonics, with the potential to revolutionize how we manipulate and use light in various technologies.

An experimental plamonic filter is presented on fig 1.5

1.5 Our approach

The two most prevalent structures for plasmonic waveguides are Metal-Insulator-Metal (MIM) and Insulator-Metal-Insulator (IMI). Although IMI structures have lower losses, MIM structures have stronger confinement of electromagnetic wave. A depiction of MIM structure is given in fig 1.6. The mid-infrared spectral range is an up-and-coming area for research

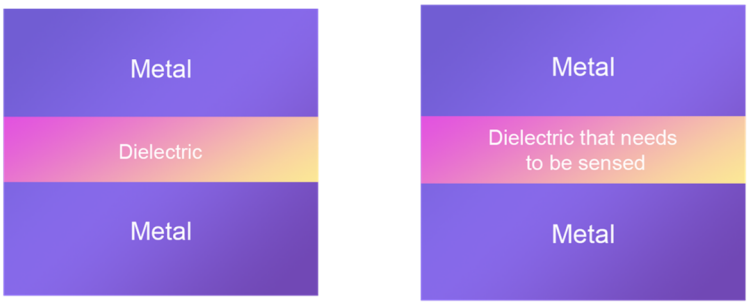

Figure 1.6: A typical MIM configuration

and development in optical sensor technology. As analytes have stronger absorption in the mid-infrared (MIR, 2.5–20 µm) band, instead of using a bulky and costly Fourier transform infrared (FTIR) spectrometer, an on-chip optical waveguide sensor can be a low-footprint replacement [38]. Lab-on-a-chip (LOC) integrates many laboratory procedures into a single apparatus, streamlining laboratory work by lowering the effort required for each technique. In Lab-on-a-chip applications, RI sensors can be used because of their low footprint, portability, rapid response, low cost, automation of laboratory operations, minimal sample volume, and detection capability without fluorescent labeling. The large size of the tag, UV-visible range restriction, pH sensitivity, limited yield, and integration of reactive groups are some of the difficulties associated with fluorescent labeling [39]. By introducing different analytes into the cavity, the effective RI (n_{eff}) will vary, resulting in a change in plasmon characteristics, which in turn will result in a change in the resonant wavelength (λ_{res}) shown in fig 1.7. The linear relationship between the refractive index and resonant wavelength is a crucial characteristic that is frequently utilized. If the electromagnetic wave stimulates the electron cloud at its resonant frequency, the light is absorbed and the particle responds strongly shown in fig 1.8. Although MIM RI sensors are less sensitive than micron-sized optical fiber and photonic crystal devices, their small footprint makes them a desirable option for lab-on-a-chip applications. That is why increasing the sensitivity of these MIM sensors have received much attention. Although much research has been done on silver-based RI sensors, many of the publications lack in the following areas: 1) Using the Drude model for material modeling, 2) Oxidation problem of silver, 3) Lack of comprehensive fabrication technique, 4)

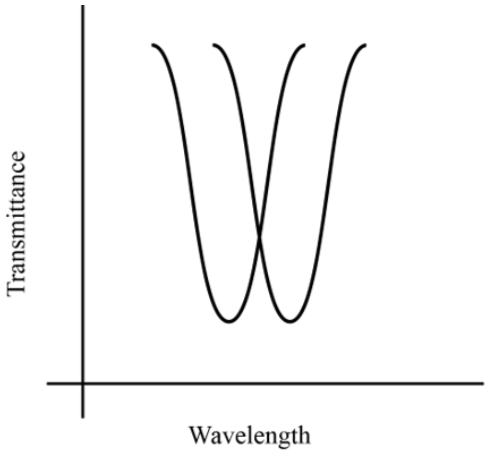

Figure 1.7: As the refractive index of the material that needs to be sensed varies, the resonant wavelength varies.

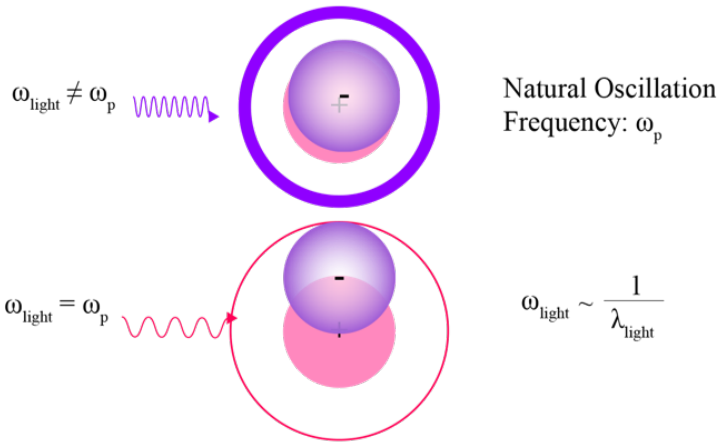

Figure 1.8: Sensing Mechanism

More diverse application. Let us focus on these lackings. While the Drude model produces almost correct results when modeling a waveguide, it does not provide reliable results when a resonator is included in the plasmonic structure. Palik and Drude–Lorentz models provide relatively comparable findings; however, the Drude model, which is widely used in many scientific articles, is unsuitable for simulating resonators, and the transmittance is reduced to half of its original value [40]. Gold has more chemical stability, electron mobility, and biocompatibility than silver, while silver is chemically unstable and, due to rapid oxidation, loses its plasmonic properties enduringly [41]. To address these issues, in this article, we propose nano dots incorporated gold-based hexagonal MIM refractive index sensor with round edges for on-chip sensing application with low-footprint. The sensor is capable of 1) detecting the concentration of protein in the cell, 2) protein solution (bovine serum albumin) concentration determination, 3) salinity in seawater determination, 4) tissue classification, and 5) temperature change detection. Previously such a wide range of on-chip novel appli-

cations have not been investigated.

1.6 Thesis Objective

1. Address the limitations observed in Refractive Index (RI) sensors based on silver. These limitations include the use of the Drude model for material modeling, problems with silver oxidation, the lack of a comprehensive fabrication technique, and the need for a wider range of applications.

2. Propose a solution to the identified limitations by developing a gold-based hexagonal Metal-Insulator-Metal (MIM) refractive index sensor with round edges that incorporates nano dots for on-chip sensing applications.

3. Demonstrate the potential of the proposed sensor in a wide range of novel on-chip applications. These include detecting the concentration of protein in cells, determining the concentration of protein solution (specifically bovine serum albumin), measuring salinity in seawater, classifying tissues, and detecting temperature changes.

4. Validate the sensor's effectiveness by presenting its achieved sensitivities in the different applications mentioned, which have not been investigated in such a wide range previously.

1.7 Thesis Layout

Chapter 1 of this book This article provides a concise yet insightful overview of Surface Plasmon Polaritons (SPPs), their usefulness, the MIR sensing region importance. It explores the mechanisms of devices that operate on SPPs and sheds light on various waveguide strategies and devices. In addition, it provides an introduction to the concepts of Plasmonics, including plasmonic waveguides and other devices like logic gates, absobers, splitters and filters.

The chapter 2 provides a comprehensive overview of diverse plasmonic refractive index sensors. It discusses their applicability in nanotechnology and optical sensing, as well as their operational principles and comparisons of various varieties. This literature review is intended to provide readers with a thorough comprehension of these innovative detection and measurement instruments.

Chapter 3, entitled "Methodology," describes the strategies and procedures used to investigate the efficacy and applications of plasmonic refractive index sensors. It provides a road map for the scientific investigation presented in this work by discussing

the research design, data collection techniques, and analysis techniques used to evaluate the sensors. This chapter not only explains the research process, but also justifies the chosen methods, ensuring the validity and reliability of the study.

Chapter 4 takes a multifaceted approach to resolving specific issues in silver-based Refractive Index (RI) sensors. The chapter proposes a novel solution: the creation of a hexagonal Metal-Insulator-Metal (MIM) refractive index sensor based on gold. With its rounded margins and nano dot integration, this sensor is designed for on-chip sensing applications. This chapter demonstrates the applicability of this innovative sensor to a range of on-chip applications. These include the detection of protein concentration in cells and solutions, the measurement of salinity in seawater, the classification of tissues, and the detection of temperature changes. The chapter concludes by demonstrating the efficacy of the proposed sensor by discussing the sensitivities it has attained in the aforementioned applications. It emphasizes that such a broad spectrum of applications has not previously been explored, illustrating the innovative nature of this research.

The concluding chapter 5 concisely concludes the study by summarizing its key findings, insights, and contributions. It revisits the limitations identified in silver-based Refractive Index (RI) sensors and explains how the proposed gold-based hexagonal Metal-Insulator-Metal (MIM) sensor offers an innovative solution to these issues. This chapter also summarizes the demonstrated potential of the new sensor for a wide range of on-chip applications, including protein concentration detection, salinity measurement, tissue classification, and temperature sensing. It concludes by highlighting the successes in sensor sensitivity across these applications and asserting the significance of these findings within the context of plasmonics and nanotechnology as a whole. This chapter provides not only a comprehensive summary, but also points at potential future research directions inspired by this study.

Chapter 2

Literature Review

In the 1940s, the Electronic Numerical Integrator and Computer (ENIAC) was among the earliest electronic general-purpose computers. It was Turing-complete, digital, and capable of being reprogrammed to address a wide variety of computing issues. By today's standards, ENIAC was colossal. It spanned 1,800 square feet and utilized approximately 18,000 vacuum tubes and 1,500 relays, weighing roughly thirty tons [42]. However, the enormous device lacked the processing speed and computational capacity required for modern computer applications [43].

Copper interconnects are limited in the number of bits that can be transmitted per second between electronic components. The physics of resistive loss gives rise to this limit, which is scale-invariant, meaning that neither expanding nor contracting the system significantly alters the limit [44]. Optical interconnects allow for high-speed communication, but because fiber optic cables are 1,000 times larger than electronic components, it was difficult to combine them with electronic components in a single circuit [45]. Surface Plasmon Polaritons (SPPs) come into play here. Since the late 1980s, surface plasmon-based sensors have been the subject of extensive research. In 1989, Batchelder et al. presented an optical sensor based on SPR that can detect specific materials [46]. Lavers et al. (1994) and Harris et al. (1995) integrated dielectric and metal coatings with a planar optical waveguide to support an SPR-based sensor for an aqueous environment and to detect a change in transmitted power, respectively. Late in the 1990s, additional integrated optical surface plasmon resonance (SPR) sensors were demonstrated [47–51]. On top of integrated optical waveguide systems, thin metal films were deposited as a substrate for the attachment of sensing films. These SPR sensors were constructed from dielectric materials with a low refractive index contrast; consequently, their dimensions were too large for lab-on-a-chip applications. Few other SPP sensors based on various detection schemes have been demonstrated. Examples include SPP resonance of nanoparticles [52, 53], and enhancement of transmission through nanohole arrays [54, 55]. In 2008, Vesseur et al. demonstrated the fabrication of gold nano-resonators

using focused-ion-6 beam milling for SPP [56].

In the discipline of nanoscale electronics, Surface Plasmon Polaritons (SPPs) are being investigated as an alternative to traditional copper interconnects. The possible benefits of utilizing SPPs for this purpose are several. Firsly, SPPs can have dimensions much smaller than the wavelength of light, potentially enabling for much higher data densities than copper. Secondly, SPPs can travel at speeds close to that of light, potentially enabling faster data transmission than is conceivable with copper. Also, SPPs can be readily integrated with existing optical systems, such as fiber optic cables, that are already utilized for high-speed data transmission over long distances. Finally, SPPs may be more energy-efficient than copper, especially as devices continue to diminish and copper wire resistance rises. Nevertheless, the use of SPPs for data transmission is not devoid of significant obstacles. These include loss (SPPs tend to dissipate over short distances), difficulty in generating and detecting SPPs, and the need for novel materials and fabrication techniques [57].

Due to the ability to support surface plasmon resonances, gold and silver are both conventionally used for metals in plasmonic sensors, but each has its own advantages and disadvantages. Silver has a more negative real part and a smaller imaginary part of the dielectric function in the visible spectrum when comparing with gold, so it can provide plasmonic sensors with greater field enhancement and sensitivity. Silver is susceptible to oxidation and sulfation in air, which degrades its optical properties with time. Gold, on the other hand, is chemically stable and resistant to oxidation and tarnishing, which makes it more suitable for long-term applications or severe environments. In addition, gold's plasmon resonance is more extensive, which can be advantageous for applications requiring a broad spectral response. Furthermore, gold is biocompatible, making it the material of choice for biological and medical applications. Gold nanoparticles are utilized extensively in biosensing, drug delivery, and photothermal therapy, among other applications [58]. Silver may be more sensitive, but gold's chemical stability, biocompatibility, and wider resonance make it a more versatile material for plasmonic sensors, particularly in biological and medical applications.

According to Becker, J. et al. the four parameters to consider when designing an 'optimal plasmonic sensor' are sensitivity, figure of merit, generalized figure of merit and figure of merit for thin layers [59]. Sensitivity is defined as the ratio of the change in the response of the sensor to a given modification in the parameter being observed. In the context of plasmonic sensors, this phenomena typically refers to the change in the sensor's optical response, such as the wavelength or intensity of the light, for a given change in the refractive index of the ambient medium, which can be caused by the presence of the target analyte. High sensitivity is desirable because it enables the detection of smaller changes in analyte concentration, which can be crucial for applications such as disease diagnosis or environmental monitoring in which the analyte may be present in extremely low concentrations. Figure of Merit (FOM) is a dimensionless quantity that is used to compare the performance

of different sensors. For plasmonic sensors, the FOM is often defined as the sensitivity divided by the full width at half maximum (FWHM) of the resonance peak in the sensor's optical response [27]. The FWHM is a measure of the resonance's bandwidth, and a smaller FWHM means a sharper resonance, which can improve the sensor's ability to distinguish between different analytes or different concentrations of the same analyte. Therefore, a higher FOM, which can be achieved by having a high sensitivity and/or a small FWHM, indicates a better performing sensor. Sensitivity and FOM are essential quality analysis parameters for plasmonic devices used in sensing applications. A sensor with a high FOM can accurately distinguish between different analytes or various concentrations of the same analyte, whereas a sensor with a high sensitivity enables the detection of minute changes in analyte concentration.

In 2023, Y. F. Chou Chau introduced a plasmonic RI sensor comprised of a metal-insulator-metal bus waveguide including a ring resonator semicircular in shape embedded with silver nanorods (AgNDs). The system's optical path is shorter than that of a conventional circular resonator. Additionally, the basement of the resonator confronting the bus waveguide provides more coupling, thereby the gap plasmon resonance increases among the incident light and AgNDs. It was discovered that the dimension of the AgNDs greatly affects the gap plasmon mode in the resonator, thus the sensitivity of the structure increases significantly. The designed structure can enhance the sensitivity of the device by 223,07% in comparison to its standard counterpart. The utmost calculated sensitivity was 2900 nm/RIU. [60]

Y. F. Chou Chau investigated numerically a metal-insulator-metal (MIM) plasmonic sensor incorporating two pair of coupled bowtie resonators featuring four silver barriers producing multiple modes in 2021. The proposed structure is capable of functioning as visible and near-infrared glucose and plasmonic refractive index sensors. Results of the simulation demonstrate that the introduction of silver baffles into bowtie cavities can alter the plasmon resonance modes and provide an adjustable method for boosting sensitivity and figure of merit. Across mode 1 to mode 3, the maximum sensitivity can reach 1,500.00, 1,400.00 and 1,100.00 nm/RIU and the highest figure of merit can reach 50.00, 46.67 and 36.00 /RIU. From the three modes operating in the visible and near-infrared simultaneously, the sensor achieved a sensitivity exceeding 1100 nm/RIU and a FOM that is unattainable in previously published literature [61].

In 2020, Yuan-Fong Chou Chau demonstrated a surface plasmon polariton (SPP)-based sensor with a simple structure which exhibited high sensitivity. It consisted of a metal–insulator–metal waveguide featuring a defected stub containing multiple silver nanorod defects. This sensor is intended for use in refractive index sensors and temperature sensors. Results from the simulation demonstrate that in a single segment, the presence of silver nanorod defects significantly impact on the sensitivity profile, providing another parameter of control over the nanometer-scale system response. The maximum refractive index sensitivity and temper-

ature sensitivity obtained are 5140 nm /RIU and approximately 2.05 nm/°C1 respectively, which can be enhanced by altering the stub length, defect rod radius, and the number of defects in the stub [62]

Rashid et al. introduced a refractive index nanosensor featuring a cog-shaped resonator embedded with nanorods comprised of gold and gold as the plasmonic material in 2021. To investigate the spectral characteristics of the sensor, Finite Element Method (FEM) was utilized. The results of the simulation show that a peak sensitivity of 6,227.6 nm/RIU was achieved for the optimal structure. In addition, the temperature sensing capability of the proposed sensor is evaluated with five distinct liquids, where chloroform exhibits the highest temperature sensitivity at 6.66 nm/°C. The chemical stability in addition to the adequate performance as a RI sensor and temperature sensing, the proposed design can serve as an appropriate alternative to silver-based sensors [63].

In 2021, Tathfif et al. proposed a titanium nitride (TiN)-based RI sensor comprising of a straight waveguide coupled with and a Square-Ring Resonator (SRR) and a groove. Additionally, nanoscale TiN nanoparticles were incorporated into the waveguide and groove to improve the sensing ability. Employing the Finite Element Method (FEM), both the geometric parameters and the materials were varied and the characteristics of the proposed sensor were investigated, and the optimized structure yielded a maximum sensitivity of 1074.88 nm/RIU and Figure of Merit (FOM) of 32.4. TiN provided several benefits, including oxidation resistance, optical tunability, high-temperature resistance, and being compliant with the standard Complementary Metal Oxide Semiconductor (CMOS) process of fabrication [64].

Butt conducted numerical research in 2023 on a plasmonic nano-sensor comprised of a metal-insulator-metal (MIM) waveguide being capable of tuberculosis (TB) detection in infected blood plasma. Use of two Si3N4 mode converters permits the effective transformation of the dielectric mode into the plasmonic mode. Tuberculosis (TB) is predominantly a lung infection, but it can also affect lymph nodes, bones, and the kidneys. Blood plasma infected with tuberculosis has a slightly lower refractive index than normal blood plasma. Because of this, a highly sensitive sensing device is essential. The proposed device achieves a sensitivity around 900 nm/RIU and figure of merit of 11.848 [65].

It is desirable for dielectric plasmonic sensors to have a significant spectral shift for a given quantity of analyte or as the refractive index changes. In the beginning, spherical gold particles [66, 67], were used, but they were quickly overtook by gold nanorods [68] due to their greater sensitivity to changes in refractive index [69]. In search of the optimal plasmonic sensor with this characteristic significant spectral shift for a given change in refractive index, numerous attempts have been taken, e.g., using rod-shaped gold nanorattles [70], metamaterials [71], gold nanorods with silver coating [72], and others. However, nanoparticles in the form of rods continue to be popular for plasmonic applications.

Metal-Insulator-Metal (MIM) and Dielectric-Metal-Dielectric (DMD) waveguides are two of the most prevalent waveguides used in plasmonic sensors in recent years. Metal-Insulator-Metal (MIM) waveguides are a form of plasmonic waveguide consisting of a thin layer of dielectric material (the insulator) sandwiched between two metal layers. The insulator may be composed of glass or a polymer, while the metal is typically composed of gold or silver. Dielectric-Metal-Dielectric (DMD) waveguides are comparable to metal-insulator-metal (MIM) waveguides, but instead of an outer metal layer, they have an outer dielectric layer. This indicates that the structure is comprised of a dielectric layer, followed by a metal layer, which is again followed by a dielectric layer. In both instances, light is confined at the interfaces by Surface Plasmon Polaritons (SPPs). Both MIM and DMD waveguides can confine light to sub-wavelength dimensions and are valuable for integrating high-density optical components. However, there are important distinctions. Firstly, DMD waveguides have generally lower propagation losses than MIM waveguides. This is due to the fact that the outer dielectric layers of DMD waveguides absorb less light than the outer metal layers of MIM waveguides. Also, DMD waveguides can support multiple light modes, whereas MIM waveguides typically support only one mode. This can increase the adaptability of DMD waveguides for specific applications. Meanwhile, MIM waveguides are typically simpler to fabricate than DMD waveguides, as they only require two distinct materials (a metal and a dielectric). Furthermore, DMD waveguides necessitate the use of three distinct materials (two distinct dielectrics and a metal), which can complicate the fabrication process. Because of this, MIM waveguides are frequently used in applications requiring high light confinement, such as nanoscale lasers and sensors. On the other hand, DMD waveguides are frequently employed in applications requiring lower losses or multiple modes, such as integrated optical circuits or waveguide-based photonic devices [73–76]. The term ”Lab-on-a-chip” (LOC) refers to devices that incorporate one or more laboratory functions onto a single, millimeter- to centimeter-sized chip. LOC devices are capable of managing fluid volumes as minuscule as less than picoliters. The significance of LOC plasmonic devices resides in their potential to revolutionize certain types of measurements and analyses. Firstly, LOC devices are significantly smaller than conventional laboratory apparatus, which can be advantageous in situations requiring limited space or portability. Secondly, LOC devices can incorporate multiple functions into a single device, thereby simplifying the testing process and possibly resulting in faster results. Thirdly, plasmonic devices can be extremely sensitive and provide real-time or near-real-time measurements, which are essential for applications such as medical diagnostics and environmental monitoring. Finally, due to their diminutive size, LOC devices are frequently manufactured at a lower cost than conventional laboratory apparatus. Additionally, they typically utilize less reagent, which further reduces costs. Thus, by employing lab-on-a-chip, plasmonic devices can be designed to detect a vast array of substances, ranging from gases to biological molecules, making them useful for a variety of applications [77, 78].

Table 2.1: Comparison between recent RI sensors

Ref.	Year	Setup	Structure	Plasmonic Material	Model	S (nm/RIU)	FOM
[79]	2023	MIM	Hexagonal ring resonator with slits	Ag	Drude	4571.7	63.3
[65]	2023	MIM	Rectangular hollow cavity	Au	Lorentz-Drude	900	11.84
[60]	2023	MIM	Semicircular ring resonator	Ag	-	2900	-
[80]	2023	MIM	Symmetric T-type resonators	Ag	-	1012	-
[81]	2023	MIM	Stub resonators and nano-disk resonators	Ag	Drude	725.1	91.78
[82]	2023	MIM	concentric ring and disk resonator	Ag	Drude	1039	401
[83]	2022	MIM	Hexagonal irregular ring resonator	Ag	Drude	2417	38
[84]	2022	MIM	r-Shaped Resonator	Ag	Debye-Drude	1333	-
[85]	2022	MIM	Semi-circular resonant cavity and a circular split-ring resonator	Ag	Drude	579	12.46
[21]	2022	MIM	U-shaped ring resonator	Ag	Debye-Drude	2020	53.16
[86]	2022	MIM	Graded 4-step waveguide	Ag	Drude	1078	-
[10]	2022	MIM	Whistle-Shaped Cavity	Ag	Debye-Drude	1229	-
[87]	2022	Grating	Compact high-index-coated polymer waveguide	PMMA	-	861	308.2
[11]	2022	Grating	Racetrack Microring Resonators	Si	-	7061	-

Table 2.1: Comparison of previous RI sensors (continued)

Ref.	Year	Setup	Structure	Plasmonic Material	Model	S (nm/RIU)	FOM
[17]	2022	MIM	Square split-ring resonator	Ag	Debye-Drude	1290.2	-
[88]	2022	Stacked Au-SiO_2-Graphene	Disk and hollowed square with four arms graphene layer	Graphene	-	817.5	76.5
[89]	2022	Metasurface	Double split ring	Graphene	-	5000	-
[63]	2021	MIM	Cog shaped resonator	Au	Lorentz-Drude	6227.6	-
[64]	2021	-	Square-ring resonator	TiN	Drude-Lorentz	1074.88	32.4
[61]	2021	MIM	Four coupled bowtie resonators	Au	Drude	1500	50
[90]	2021	MIM	Unequal vertical rectangular cavities	Ag	Lorentz-Drude	2625.87	26.04
[19]	2021	MIM	Asymmetric ring cavity	Au	-	440.2	52.6
[91]	2021	MIM	Pentagonal ring resonator	Ag	Lorentz-Drude	2325	46
[27]	2021	MIM	Triangular resonator	Ag	Lorentz-Drude	2713	35.1
[92]	2021	Grating	Complementary grating	Au/Si	Drude	1642	409
[93]	2021	MIM	U-shaped cavity	Ag	Debye-Drude	825	21.54
[94]	2021	MIM	Elliptical resonator	Ag	Drude	550	282.5
[62]	2020	MIM	Stub including several silver nanorod defects	Ag	-	5140	-

Table 2.1: Comparison of previous RI sensors (continued)

Ref.	Year	Setup	Structure	Plasmonic Material	Model	S (nm/RIU)	FOM
[7]	2020	MIM	Bow Tie configuration	Ag	Lorentz-Drude	2300	
[95]	2020	MIM	Double concentric square ring resonator and stubs	Ag	Drude	1270	58
[96]	2020	MIM	Dual channel	Ag	-	1940	2235
[97]	2020	MIM	Disk resonator	Ag	Drude	1261.67	-
[16]	2020	MIM	Semicircular resonant cavity coupled with a key-shaped resonant cavity	Ag	Drude	1261.67	-
[98]	2020	MIM	Square ring resonator with nanodots	Ag	Debye-Drude	1240	20
[99]	2020	MIM	Dual-band tunable absorber	Ag	Drude	1240.8	44.5
[6]	2020	MIM	Square ring resonator with nanodots	Ag	Lorentz-Drude	907	50.4
[100]	2020	MIM	Elliptical cavity resonator	Ag	Drude	540	101.3
[9]	2020	MIM	Dual rectangular cavity system	Ag	Drude	701	-
[15]	2020	Grating	Nano-array with rhombus particles	Au	Drude	1006	305.7
[101]	2020	MIM	Dumble shaped cavity slots	Ag	Drude	1260	120
[102]	2020	-	Two concentric double square resonator	Au	Lorentz-Drude	1380	104
[22]	2020	-	Concentric double ring resonators	Ag	Drude	1516	14.83

Table 2.1: Comparison of previous RI sensors (continued)

Ref.	Year	Setup	Structure	Plasmonic Material	Model	S (nm/RIU)	FOM
[103]	2019	MIM	Tooth cavity-coupled ring splitting cavity	Ag	Debye-Drude	1200	-
[20]	2019	MIM	Triangular and circular cavity	Ag	Debye-Drude	1500	65.2
[8]	2019	MIM	Two horizontal cavity	Ag	-	1382	35.3
[104]	2019	Grating	Racetrack resonator	Si	-	1550	2000
[12]	2019	Array film	Y-shaped arrays	Ag	-	900	-
[14]	2019	-	Nanocubes	Au	Drude	1002	417
[105]	2019	Stacked graphene sheets	Asymmetric double graphene layers	Graphene	Drude	1900	-
[106]	2018	MIM	Elliptical ring resonator	Ag	Drude	1100	224
[18]	2018	MIM	U-shaped resonator	Ag	Drude	917	180
[107]	2018	MIM	Ring resonator	Ag	Drude	1383	93.1
[108]	2018	MIM	Square type split ring resonator	Ag	Drude	1700	60.7
[13]	2018	Periodic surface	Nano-rods	In tin oxide	-	1587	-
[109]	2018	MIM	Octagonal ring cavity	Ag	Drude-Lorentz	1540	-
[5]	2018	MIM	Double side-coupled square ring resonators	Ag	Drude	806	66

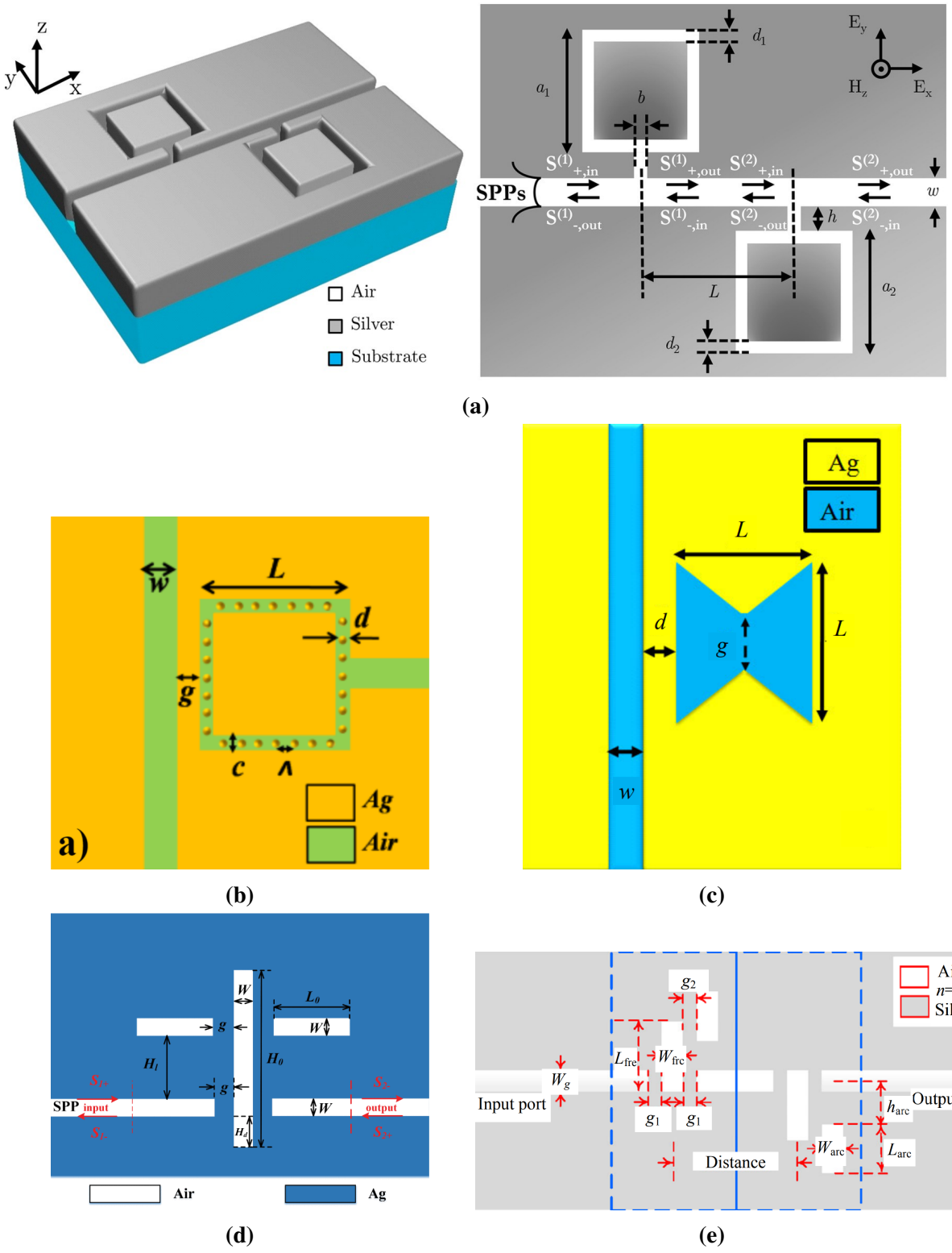

Figure 2.1: Recently published RI sensors (a) Akhavan et al. [5] (b) Butt et al. [6] (c) Butt et al. [7] (d) Li et al. [8] (e) Li et al. [9]

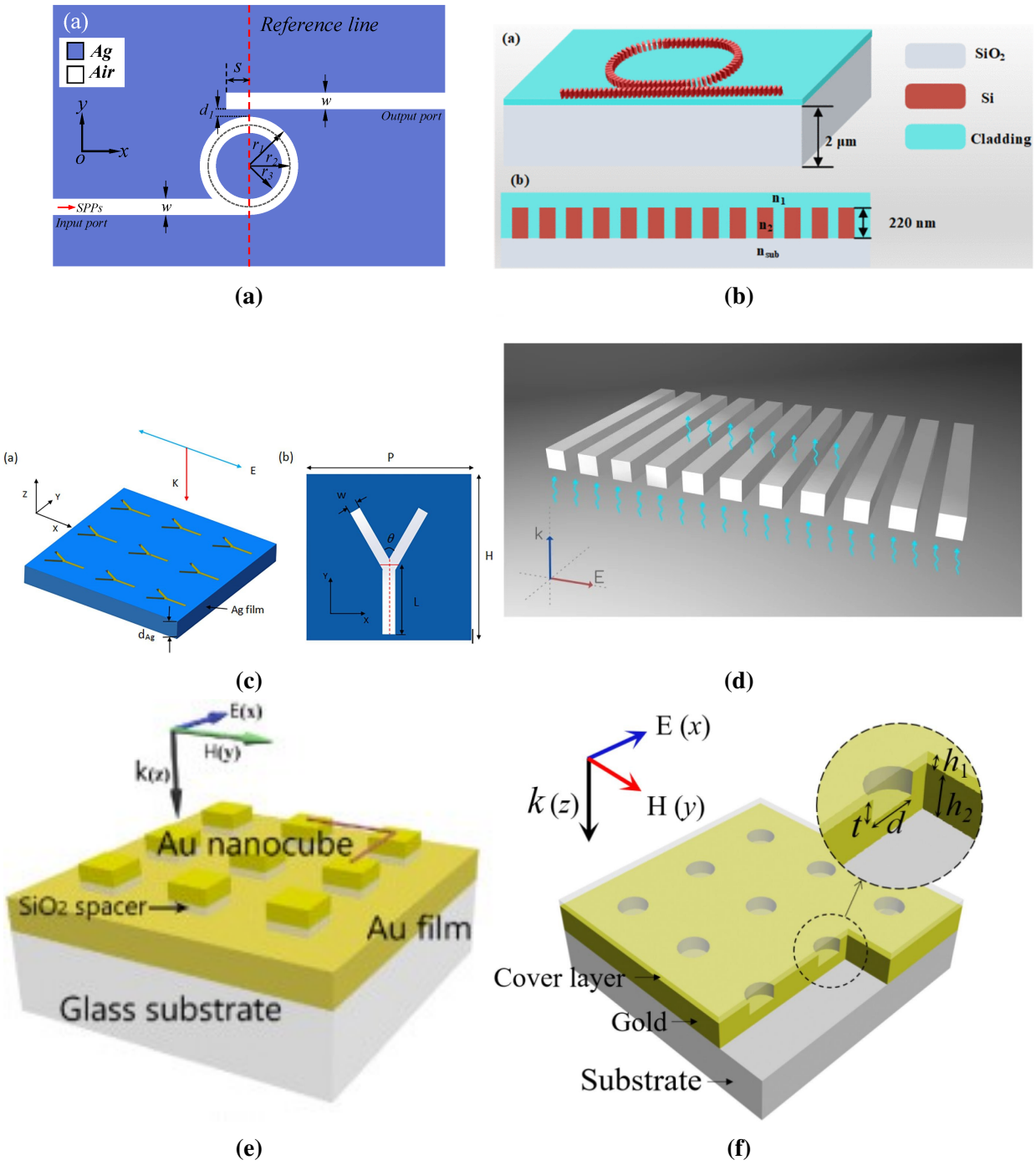

Figure 2.2: Recently published RI sensors (a) Li et al. [10] (b) Liu et al. [11] (c) Qi et al. [12] (d) Rashed et al. [13] (e) Wang et al. [14] (f) Yu et al. [15]

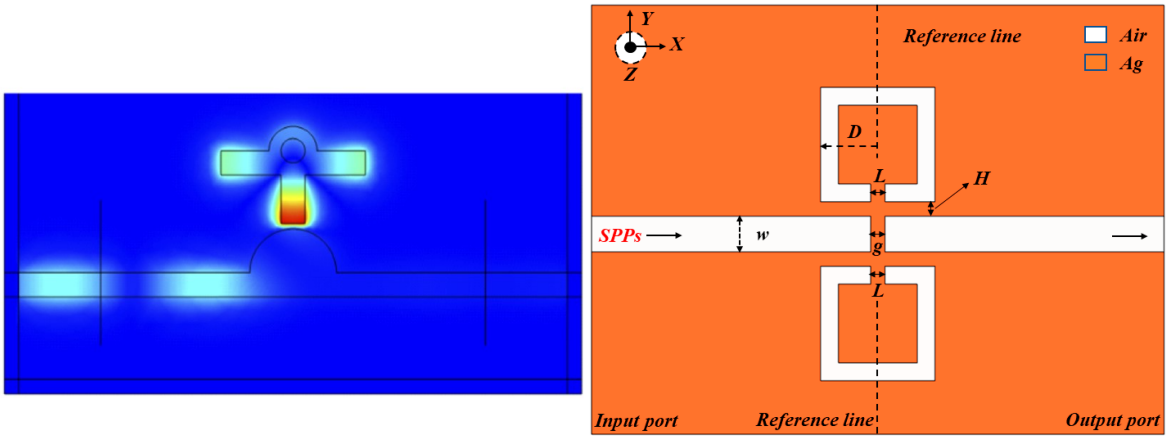

(a) (b)

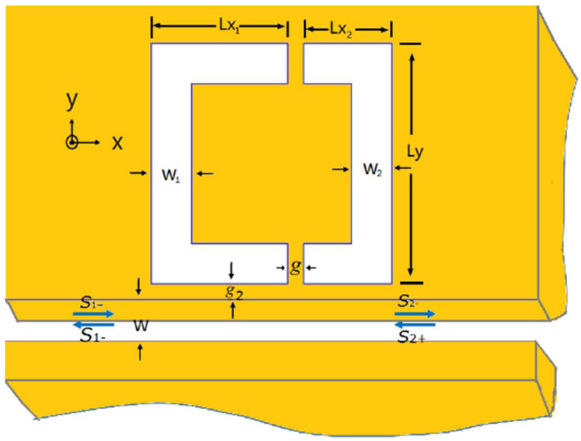

(c)

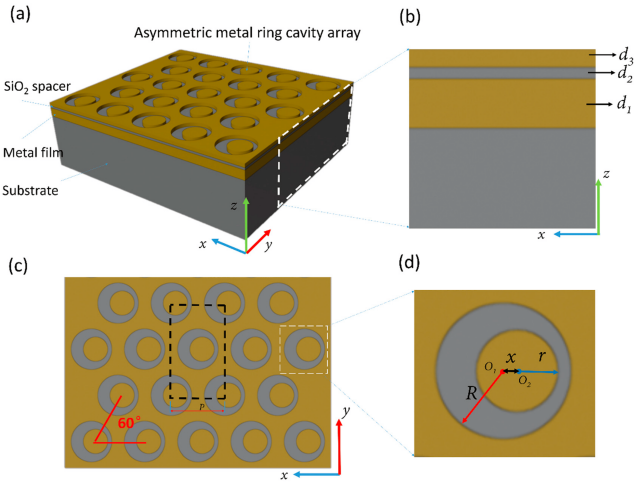

(d)

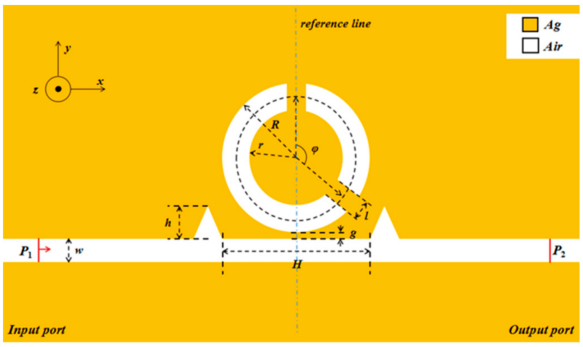

(e)

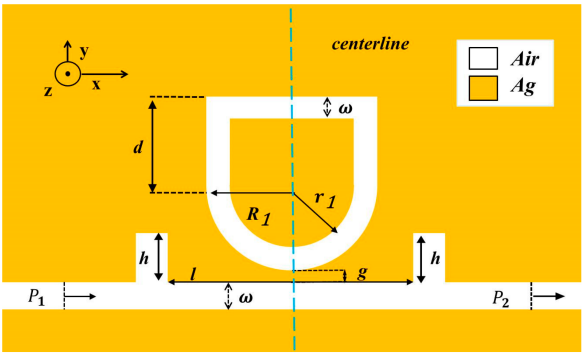

(f)

Figure 2.3: Recently published RI sensors (a) Zhu et al. [16] (b) Chen et al. [17] (c) Ren et al. [18] (d) Xu et al. [19] (e) Yang et al. [20] (f) Zhang et al. [21]

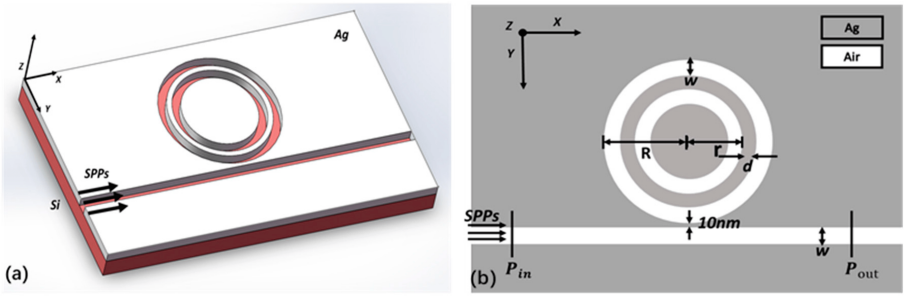

Figure 2.4: Recently published RI sensor (a) Zhang et al. [22]

Table 2.1 highlights some recently published refractive index sensors and compares them with the metrics Sensitivity and FOM.

Among the highlighted plasmonic sensors, 2.1 (a-e), 2.2 (a-f), 2.3 (a-f) and 2.4 (a) vizualizes some of them.

Chapter 3

Methodology

3.1 Wave Theory

In this section of our study, we explore the theoretical basis for our innovative oxidation-resistant nanosensor design. Utilizing a metal-insulator-metal structure and surface plasmon resonance for sensing, the operation of this sensor is dependent on a thorough comprehension of Maxwell's equations and constitutive relations. It is impossible to overstate the importance of these equations and their derivations in the field of electromagnetism and optical physics, given their central role in characterizing the interaction between electromagnetic fields and matter.

3.1.1 Maxwell's Equations

The four equations of Maxwell are a comprehensive mathematical description of electromagnetic phenomena. They consist of the Gauss laws for electric and magnetic fields, the Faraday law of electromagnetic induction, and Ampere's law with Maxwell's addition. Our sensor technology is founded on the profound implications of these equations, which explain the propagation of light and predict the existence of electromagnetic waves.

1. Gauss's Law for Electricity: This law describes the relationship between a static electric charge and the electric field it produces. The law states that the electric flux through a closed surface is proportional to the total charge enclosed by the surface. Mathematically, this is expressed as,

$$\nabla \cdot \mathbf{E} = \frac{\rho}{\epsilon_0} \tag{3.1}$$

where $\mathbf{E}$ represents the electric field, ρ is the electric charge density, and ϵ_0 is the permittivity of free space.

2. Gauss's Law for Magnetism: This law asserts that there are no magnetic monopoles in nature, i.e., magnetic fields emanate from 'north' poles and terminate at 'south' poles, always forming closed loops. Thus, the net magnetic flux through any closed surface is zero. Mathematically, this is expressed as,

$$\nabla \cdot \mathbf{B} = 0 \tag{3.2}$$

where $\mathbf{B}$ is the magnetic field.

3. Faraday's Law of Electromagnetic Induction: This law demonstrates that a time-varying magnetic field produces an electric field that forms closed loops, a phenomenon known as electromagnetic induction. Mathematically, this is expressed as,

$$\nabla \times \mathbf{E} = -\frac{\partial \mathbf{B}}{\partial t} \tag{3.3}$$

where $\frac{\partial \mathbf{B}}{\partial t}$ represents the rate of change of the magnetic field with respect to time.

4. Ampere's Law with Maxwell's Addition: Ampere's Law, as amended by Maxwell, states that a time-varying electric field, along with electric current, generates a magnetic field. Mathematically, this is expressed as,

$$\nabla \times \mathbf{B} = \mu_0 \mathbf{J} + \mu_0 \epsilon_0 \frac{\partial \mathbf{E}}{\partial t} \tag{3.4}$$

where $\mathbf{J}$ is the current density, and μ_0 and ϵ_0 are the permeability and permittivity of free space, respectively.

3.1.1.1 Wave Equation

The wave equation is a key mathematical tool for understanding how waves propagate through space. Electromagnetic waves, which are a central aspect of the operation of our nanosensor, are governed by a wave equation derived from Maxwell's equations. The following derivation outlines how this wave equation is obtained.

For simplicity, let's consider the case in a source-free region (i.e., where the charge density $\rho = 0$ and current density $J = 0$). This simplifies Ampère's Law to,

$$\nabla \times B = \mu_0 \epsilon_0 \frac{\partial E}{\partial t} \tag{3.5}$$

Taking the curl of both sides of Faraday's law gives,

$$\nabla \times (\nabla \times E) = -\frac{\partial}{\partial t}(\nabla \times B) \tag{3.6}$$

Using the vector identity $\nabla \times (\nabla \times E) = \nabla(\nabla \cdot E) - \nabla^2 E$, and recalling that $\nabla \cdot E = 0$ in a source-free region, we get,

$$-\nabla^2 E = -\frac{\partial}{\partial t}(\nabla \times B) \tag{3.7}$$

Substituting Ampère's law into this equation, we get,

$$\nabla^2 E = \mu_0 \epsilon_0 \frac{\partial^2 E}{\partial t^2} \tag{3.8}$$

This is the wave equation for the electric field E in a source-free region. Similarly, by taking the curl of Ampère's law and proceeding in the same way, we can derive the wave equation for the magnetic field B,

$$\nabla^2 B = \mu_0 \epsilon_0 \frac{\partial^2 B}{\partial t^2} \tag{3.9}$$

These wave equations govern the propagation of electromagnetic waves in free space. The speed of propagation of these waves, c, is given by $\frac{1}{\sqrt{\mu_0 \epsilon_0}}$.

3.1.2 Constitutive Equations

The constitutive equations express the relation between electromagnetic field and our nanosensor's material hence they are crucial in understanding the nanosensor's workings. These equations establish the connection between electromagnetic field and the material's response to it, providing key insights into the behavior of the materials under different field conditions.

The primary constitutive relations in electromagnetism are: Electric Displacement Field (D), Electric Field (E), and Electric Polarization (P): This relationship is defined as,

$$D = \varepsilon_0 E \tag{3.10}$$

where ε_0 is the free space permittivity of the material. Permittivity is a measure of a material's ability to store electrical energy in an electric field.

The polarization of a material refers to the separation of charges within a dielectric material under an external electric field. This is expressed as,

$$P = \chi_e \varepsilon_0 E \tag{3.11}$$

for linear, isotropic, and homogeneous materials, where χ_e is the electric susceptibility of the material.

Hence, when materials are subjected to an electric field, the electric displacement becomes,

$$D = \varepsilon_0 E + \chi_e \varepsilon_0 E \tag{3.12}$$

Thus we get,

$$D = \varepsilon_0 \varepsilon_r E \tag{3.13}$$

where the relative electric permittivity of the material is given by, $\varepsilon_r = 1 + \chi_e$

Magnetic Field (H) and Magnetic Field Strength (B), and Magnetization (M): This relation is defined as,

$$B = \mu_0 H \tag{3.14}$$

where μ_0 is the free space permeability of the material. Permeability quantifies a material's ability to conduct a magnetic field.

Analogous to electric polarization, we also have a concept of magnetic polarization or magnetization (M) in response to an applied magnetic field. Thus, the full relationship between H and B includes this magnetization component, given as,

$$B = \mu_0 (H + M) \tag{3.15}$$

where μ_0 is the permeability of free space. For linear, isotropic, and homogeneous materials, we can write,

$$M = \chi_m H \tag{3.16}$$

where χ_m is the magnetic susceptibility of the material. Thus, we get,

$$B = \mu_0 \mu_r H \tag{3.17}$$

where the relative permeability of the material is given by, $\mu_r = 1 + \chi_m$

Current Density (J) and Electric Field (E): The relationship is expressed by,

$$J = \sigma E \tag{3.18}$$

where σ is the conductivity of the material, indicating how readily the material allows the flow of electric current.

3.1.3 General Constitutive Equations

While the standard constitutive equations provide a robust framework for understanding the behavior of materials under the influence of electric and magnetic fields, they are largely sim-

plified, assuming linearity, isotropy, and homogeneity. However, many materials, especially those used in sophisticated devices like our nanosensor, exhibit more complex behaviors. To account for these complexities, we use generalized constitutive equations.

The standard constitutive equations we discussed in the previous section assume that the material's permittivity is applied field's direction independent and linear. However, in reality, many materials' permittivity is anisotropic and nonlinear.

For anisotropic materials, their permittivity can be expressed by a tensor of 9 components. As such, the electric field equation becomes,

$$\begin{bmatrix} D_x \\ D_y \\ D_z \end{bmatrix} = \begin{bmatrix} \varepsilon_{xx} & \varepsilon_{xy} & \varepsilon_{xz} \\ \varepsilon_{yz} & \varepsilon_{yy} & \varepsilon_{yz} \\ \varepsilon_{zx} & \varepsilon_{zy} & \varepsilon_{zz} \end{bmatrix} \begin{bmatrix} E_x \\ E_y \\ E_z \end{bmatrix} \tag{3.19}$$

The same applies to the current density and electric field equation. The conductivity σ can be expressed by a tensor of 9 components similar to electric permittivity.

3.2 Material Modeling

Material modeling is a crucial aspect of our study. It provides the theoretical basis for comprehending and predicting the behavior of metal-light interaction and surface plasmon resonance. The three models that we utilize for this purpose are the Drude model, the Lorentz model, and the Lorentz-Drude model. Each of these models provides a unique perspective on the response of electrons in a material to an applied electric field, which is essential to understanding how our nanosensor operates.

3.2.1 Lorentz Model

The Lorentz model is used to describe the behavior of bound electrons in a solid. Unlike the Drude model, the Lorentz model assumes that electrons are bound to atoms and oscillate around their equilibrium positions. When an external electric field is applied, the electrons' equilibrium positions are displaced. It is assumed that the restoring force that returns the electron to its equilibrium position is proportional to the displacement. In addition, there is a damping force that is proportional to the velocity of the electron, which accounts for energy loss due to collisions and other interactions. It can be compared to a spring and damper system shown in fig 3.1

We can derive an expression for the polarization of the material in terms of the external electric field by solving the equation of motion for an electron under these conditions. This

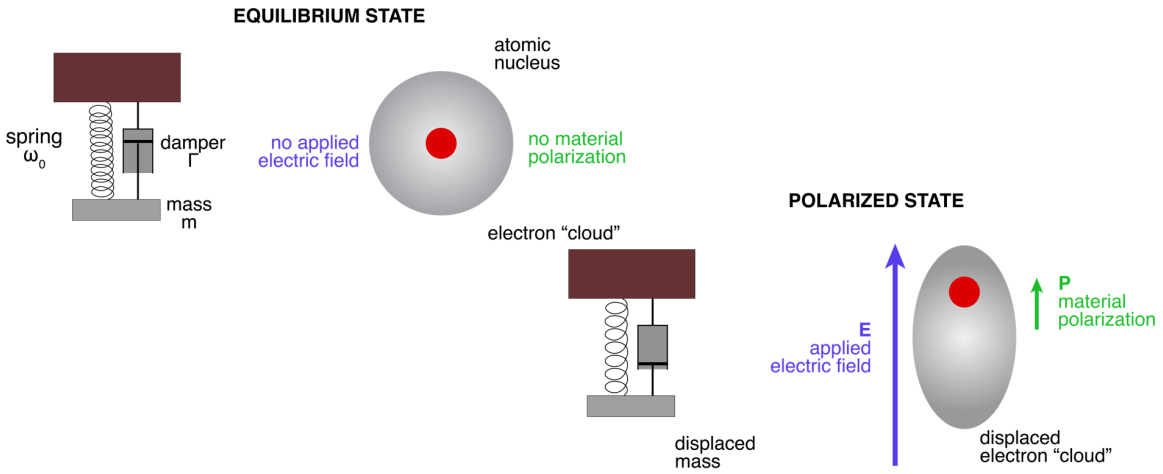

Figure 3.1: Sensing Mechanism

results in an expression for the material's electric permittivity, which characterizes its response to an electric field.

The equation of motion for an electron under the influence of an external electric field $E(t)$ is given by:

$$m\frac{d^2x}{dt^2} = -eE(t) - m\gamma\frac{dx}{dt} - m\omega_0^2 x \tag{3.20}$$

where:

- m is the mass of the electron,
- e is the charge of the electron,
- $E(t)$ is the external electric field,
- γ is the damping constant,
- x is the displacement of the electron from its equilibrium position, and
- ω_0 is the resonant frequency.

Assuming a harmonic time dependence, $E(t) = E_0 e^{-i\omega t}$, and solving the equation of motion, we get the polarization $P(\omega)$:

$$P(\omega) = \frac{ne^2}{m(\omega_0^2 - \omega^2 - i\gamma\omega)}E(\omega) \tag{3.21}$$

The electric permittivity is then given by:

$$\epsilon(\omega) = 1 - \frac{\omega_p^2}{\omega_0^2 - \omega^2 - i\gamma\omega} \tag{3.22}$$

where ω_p is the plasma frequency. Expanding it [23], we have:

$$\epsilon(\omega) = 1 - \sum_{i=1}^{m} \frac{f_i \omega_i^2}{\omega_i^2 - \omega^2 + i\gamma_i \omega} \tag{3.23}$$

3.2.2 Drude Model

Paul Drude proposed the Drude model in 1900 in order to explain the electrical and thermal properties of metals. In this model, a metal is represented as a gas of free electrons moving through a sea of positive ions. The electrons are considered to be free because they do not remain fixed to the atoms and can move freely within the metal.

These electrons' mobility is affected by both an external electric field and collisions with positive ions. It is assumed that these collisions are instantaneous, random events that alter the velocity of the electrons. Between collisions, the velocity of electrons is constant.

The equation of motion for an electron under the influence of an external electric field $E(t)$ is similar to the Lorentz model with the exception that there is no restoring force component. The equation is given by,

$$m\frac{dv}{dt} = -eE(t) - m\gamma v \tag{3.24}$$

where: m is the mass of the electron, e is the charge of the electron, $E(t)$ is the external electric field, γ is the damping constant, and v is the velocity of the electron.

Assuming a harmonic time dependence, $E(t) = E_0 e^{-i\omega t}$, and solving the equation of motion, we get [23]:

$$\epsilon(\omega) = 1 - \frac{\omega_p^2}{\omega^2 - i\gamma_0 \omega} \tag{3.25}$$

where ω_p is the plasma frequency.

3.2.3 Lorentz-Drude Model

Combining the Drude and Lorentz models results in the Lorentz-Drude model. It describes the response of free and bound electrons in a solid to an external electric field. In the Lorentz-Drude model, the electric permittivity is the sum of the permittivities derived from the Drude and Lorentz models. As the behavior of metals predicted by the Drude model differs from reality, the combination of the Lorentz and Drude models provides a more thorough description of the material's response to an electric field by considering both free and bound electrons.

The electric permittivity is expressed as [23]:

$$\epsilon(\omega) = 1 - \frac{\omega_p^2}{\omega^2 - i\gamma_0\omega} + \sum_{i=1}^{m} \frac{f_i\omega_i^2}{\omega_i^2 - \omega^2 + i\gamma_i\omega} \tag{3.26}$$

where ω_p is the plasma frequency and f_i is the oscillator strength.

3.2.4 Ag Modeling

In the work done by Rakic et al. [23] the 11 plasmonic materials were fit for Lorentz-Drude model. Among them there is Ag. table 3.1 lists the Lorentz-Drude parameters for Ag.

Table 3.1: Lorentz-Drude Parameters for Ag [23]

Parameters	Values (eV)
Plasma Frequency ($\hbar\omega_p$)	9.01
Collision Frequency (Γ_0)	0.048
Oscillator Strength (f_i)	[0.845; 0.065; 0.1240; 0.11; 0.840; 5.646]
Damping Frequency (γ_i)	[0.048; 3.886; 0.452; 0.065; 0.916; 2.419]
Resonant Frequency (ω_i)	[0; 0.816; 4.481; 8.185; 9.083; 20.29]

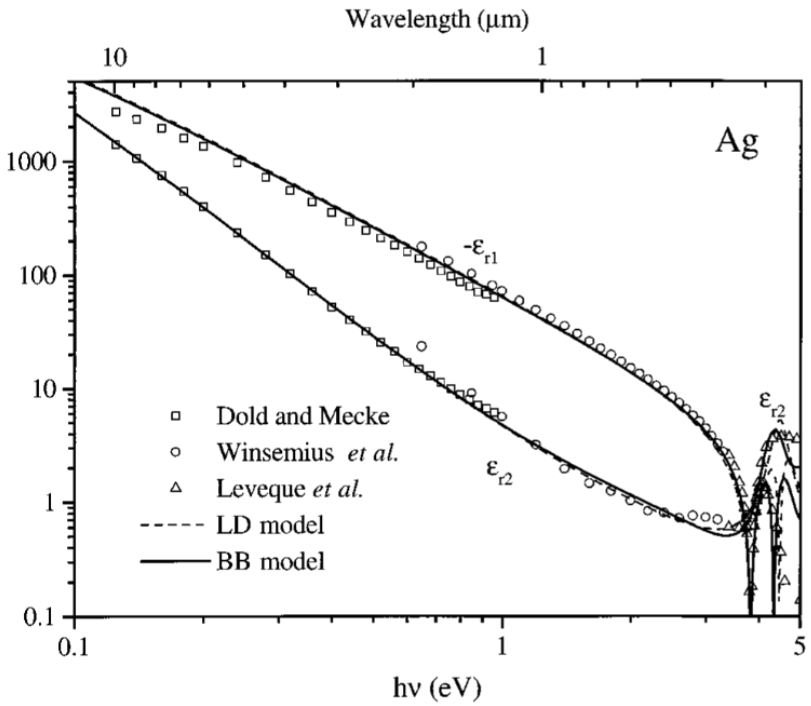

Figure 3.2: Real and complex permittivity of Ag [23].

3.2.5 Au Modeling

Au was also among the materials on which Rakic et al [23] worked. Table 3.2 lists the Lorentz-Drude parameters for Au.

Table 3.2: Lorentz-Drude Parameters for Au [23]

Parameters	Values (eV)
Plasma Frequency ($\hbar\omega_p$)	9.03
Collision frequency (Γ_0)	0.053
Oscillator strength (f_i)	[0.760; 0.024; 0.010; 0.071; 0.601; 4.384]
Damping frequency (γ_i)	[0.053; 0.241; 0.345; 0.870; 2.494; 2.214]
Resonant frequency (ω_i)	[0; 0.415; 0.830; 2.969; 4.304; 13.32]

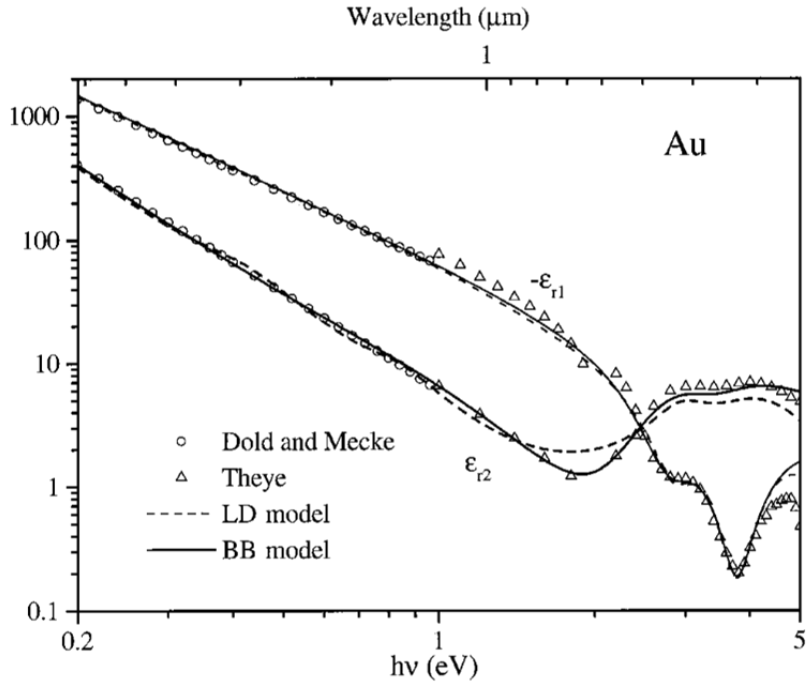

Figure 3.3: Real and complex permittivity of Au [23].

3.3 Surface Plasmon Resonance

Surface Plasmon Polaritons (SPPs) are a specific class of electromagnetic waves that propagate along the interface between a metal and a dielectric. They are generated through the coupling of incident photons with coherently oscillating electrons present at the interface [110]. This interaction results in a wave that is bound to the surface, decaying evanescently into both the metal and the dielectric [111]. The significance of SPPs lies in their ability to overcome the diffraction limit of light, a fundamental barrier in optics that restricts the resolution of conventional optical devices to approximately half the wavelength of light. This limit has

posed a significant challenge in the field of nanophotonics, particularly in the development of high-speed, miniaturized devices. SPPs, however, can confine light to sub-wavelength

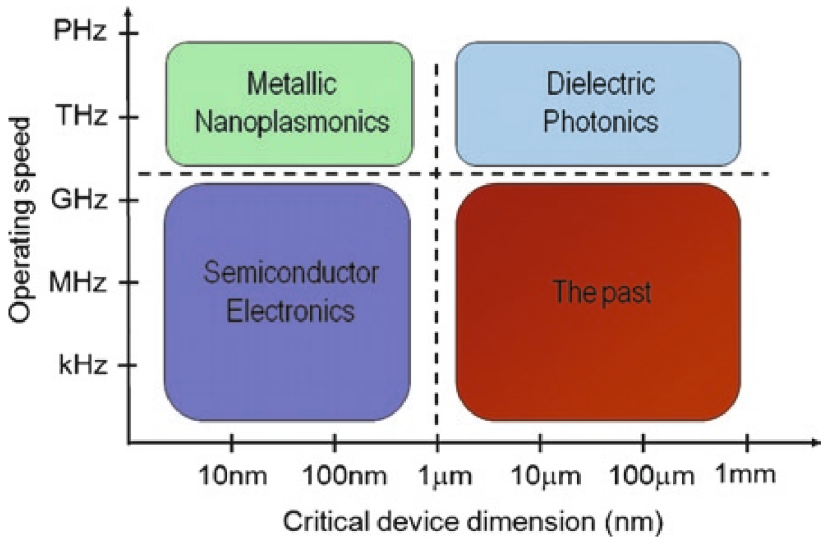

Figure 3.4: Graph of the operating speeds and critical dimensions of different chip-scale device technologies [24].

scales, effectively bypassing the diffraction limit. This confinement allows for the creation of metal-based nanoscale devices, such as directional couplers, reflectors, logic gates, demultiplexers, and refractive index sensors. By utilizing SPPs, these devices can operate at optical frequencies, enabling ultra-high-speed data processing and transmission. The ability of SPPs to confine light beyond the diffraction limit also opens up new possibilities in the field of sensing. For instance, refractive index sensors based on SPPs can detect minute changes in the refractive index, enabling the measurement of properties such as protein concentration, salinity, and even the classification of different types of tissues. This makes SPP-based devices powerful tools for various applications in biotechnology and healthcare.

3.3.1 Dispersion Relation

The dispersion relation describes how the phase velocity of a wave depends on its frequency. The dispersion relation plays an important role in the context of surface plasmon polaritons (SPPs) because it determines the propagation characteristics of these waves.

The dispersion relation for SPPs can be derived from Maxwell's equations and the boundary conditions at the metal-dielectric interface. From the combination of these two, it can be derived that [112]:

$$D_0 = \frac{k_{zd}}{\epsilon_d} + \frac{k_{zm}}{\epsilon_m} = 0 \tag{3.27}$$

where: k_{zd} is the component of the wave vector along the direction perpendicular to the interface in the dielectric, k_{zm} is the component of the wave vector along the direction per-

pendicular to the interface in the metal, ϵ_d is the relative permittivity of the dielectric, and ϵ_m is the relative permittivity of the metal.

It can be observed that for SPPs to occur, it is essential that the permittivity of the adjacent materials have opposite signs.

Additionally, the wave vector components can be expressed as:

$$\epsilon_i \left(\frac{\omega}{c}\right)^2 = k_x^2 + k_{zi}^2, \quad i = m, d \tag{3.28}$$

or

$$k_{zi} = \left(\epsilon_i \left(\frac{\omega}{c}\right)^2 - k_x^2\right)^{\frac{1}{2}}, \quad i = m, d \tag{3.29}$$

where k_x is the continuous wave vector component along the interface direction due to boundary conditions.

The dispersion relation can then be derived as:

$$k_x = \frac{\omega}{c}\left(\frac{\epsilon_m \epsilon_d}{\epsilon_m + \epsilon_d}\right)^{\frac{1}{2}} \tag{3.30}$$

As the refractive index of the metal varies with the frequency of light and can be negative, if $\mathrm{Re}(\epsilon_m) < \epsilon_d$, the real part of the wavevector of the SPP can be expressed as [113]:

$$\mathrm{Re}(k_{\mathrm{spp}}) = nk_0 \frac{1}{\sqrt{1 - \left|\frac{\epsilon_d}{\mathrm{Re}(\epsilon_m)}\right|}} > nk_0 \tag{3.31}$$

From which it can be inferred that the resulting wave vector of the SPP is smaller than the incident wave vector thus circumventing the problem of diffraction limit

3.3.2 Sensing Mechanism

The sensing mechanism of our oxidation-resistant nanosensor is based on the principles of surface plasmon resonance (SPR) and refractive index sensing. Our sensor is a hexagonal ring resonator that utilizes changes in the refractive index of the dielectric medium for detection purposes. Our sensor is designed as a hexagonal ring resonator, a structure that can create resonance through trapping light. As the light travels down the waveguide, it is coupled into the resonator, it can circulate multiple times around the ring, enhancing its interaction with the dielectric medium and creating opportunities for resonance at specific frequencies of light [114].

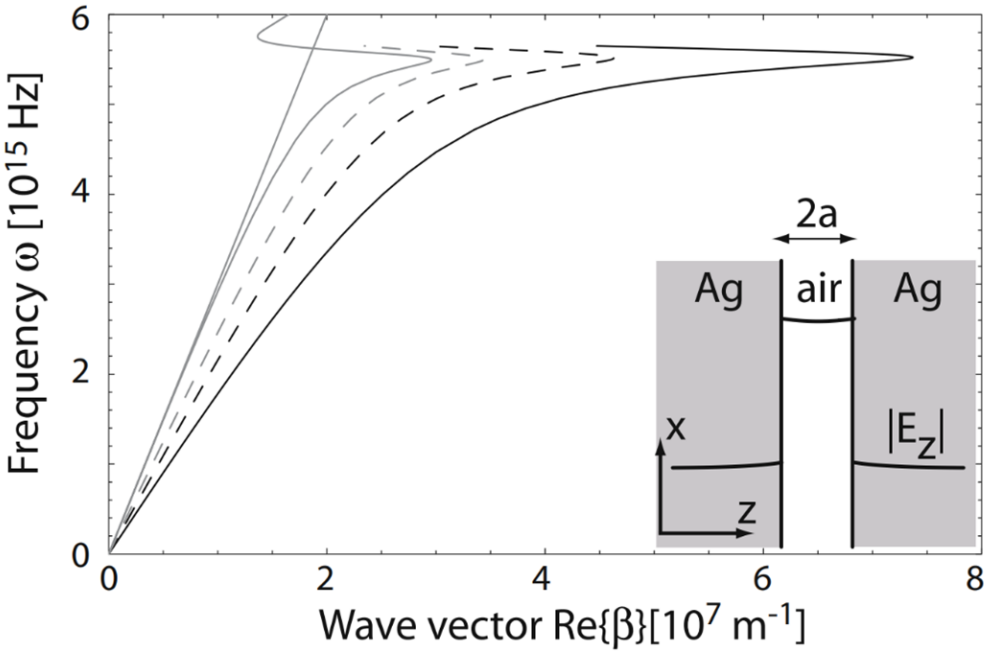

Figure 3.5: Dispersion relation of the fundamental coupled SPP modes of a silver/air/silver multilayer geometry for an air core of size 100 nm (broken gray curve), 50 nm (broken black curve), and 25 nm (continuous black curve). Also shown is the dispersion of a SPP at a single silver/air interface (gray curve) and the air light line (gray line) [25].

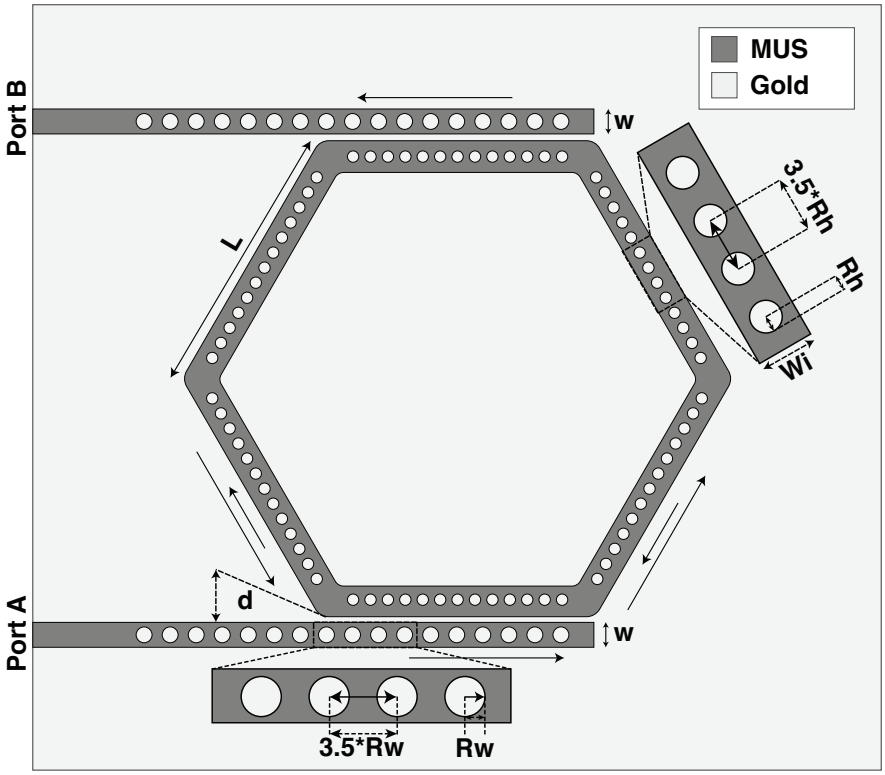

Figure 3.6: Circulation of light

The refractive index of the medium determines the resonant wavelength of the light circu-

lating in the ring. Therefore, a shift in the resonant wavelength will result from a change in the refractive index. The Maxwell's equations and boundary conditions at metal-dielectric interface can be used for calculating the effective refractive index of the MIM hexagonal ring resonator [114].

$$k_d \epsilon_m \tanh\left(\frac{k_d d}{2}\right) + \epsilon_d k_m = 0 \tag{3.32}$$

$$k_{d,m} = \sqrt{\beta_{\text{spp}}^2 - \epsilon_{d,m} k_o^2} \tag{3.33}$$

$$\eta_{\text{eff}} = \frac{\beta_{\text{spp}}}{k_o} \tag{3.34}$$

As the EM field loops back around the hexagonal ring resonator, if the effective path length of the resonator is an integer multiple of the wavelength of the EM field in the resonator, then a resonance is formed and the energy of the EM field gets trapped in the resonator. The resonant wavelength then becomes [115]:

$$\lambda_{\text{res}} = \frac{6 L_D \eta_{\text{eff}}}{m - \frac{\phi}{2\pi}} \tag{3.35}$$

where m is an integer, L_D is the length of a side of the hexagonal resonator, and ϕ is the accumulated phase gained at the bends of the structure around a round trip.

The mechanism begins by exciting a port of the sensor with a light source. The light interacts with the metal-insulator-metal structure, exciting surface plasmons at the metal-dielectric interface. The surface plasmons generate EM waves that travel down the waveguide and get coupled to the ring resonator, creating resonance at certain frequencies. If the refractive index of the medium changes, for example, due to the binding of a target molecule, the resonance condition will be altered. This change will cause a shift in the effective path of the wave by changing the effective refractive index through a change in the relative permittivity of the dielectric medium. As such, the resonant wavelength of the light circulating in the hexagonal ring resonator also changes. By monitoring this shift, we can detect the presence and concentration of the target molecule.

3.4 Simulation Method

The Finite Element Method (FEM) is a potent numerical technique used to address complex problems in a variety of disciplines, including heat transfer, fluid mechanics, mechanical systems and electromagnetics. It is especially useful for problems with a high degree of complexity and an unusual geometry, which are often very difficult to solve with analytical

methods. The method involves approximating continuous quantities as discrete quantities at discrete nodes, which are often evenly spaced across a grid or lattice. The necessity of the Finite Element Method stems from its capacity to analyze structures that are too difficult to solve analytically. It provides a systematic procedure for transforming the governing differential equations into algebraic equations that can be solved using computational techniques. The procedure consists of four major steps [26]:

3.4.1 Finite Element Discretization

The domain is discretized in the first step of the Finite Element Method. Domain discretization is accomplished by dividing the complex structure or physical domain of the solution region into a set of simpler, interconnected subdomains known as finite elements. Depending on the nature of the problem, these elements may be 1D (line), 2D (triangle, quadrilateral), or 3D (tetrahedron, hexahedron). The points where these elements connect are known as nodes. For example, in fig 3.7 the region is divided into 2 triangular and 2 quadrilateral elements,

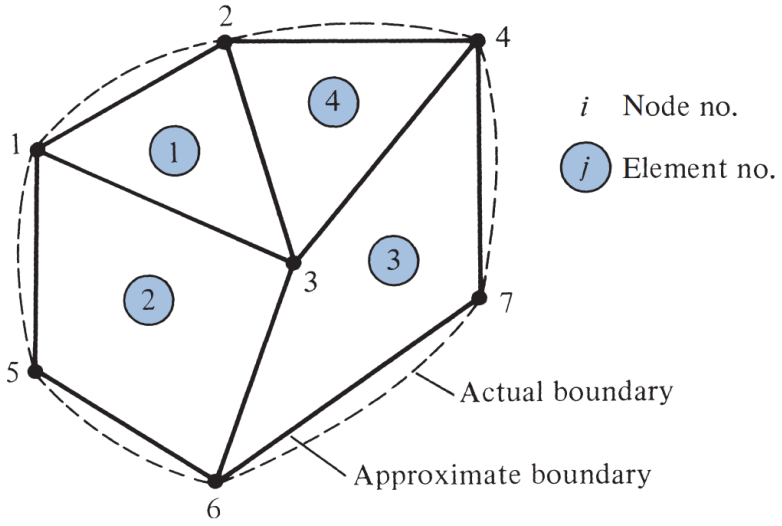

Figure 3.7: A typical finite element subdivision of an irregular domain [26].

with a total of 7 nodes. The potential V_e at various nodes is approximated iteratively such that the potential is continuous across the boundaries of different elements. The approximate solution for the whole region is given by:

$$V(x, y) \approx \sum_{e=1}^{N} V_e(x, y) \tag{3.36}$$

where N is the number of triangular elements into which the solution region is divided. For simplicity, we can assume a 1st order linear form approximation of V_e:

$$V_e(x, y) = a + bx + cy \tag{3.37}$$

The linear variation of electric potential is assumed when the electric field is uniform within the element:

$$E_e = -\nabla V_e \tag{3.38}$$

3.4.2 Element Governing Equations

This step is done by applying the governing differential equations to each element in the discretized domain. The equations are written in terms of the unknown function values at the nodes, which are represented by the shape functions. This process results in a system of algebraic equations. Let us consider a typical triangular element shown in fig 3.8 The potential at different nodes are obtained using the following equations,

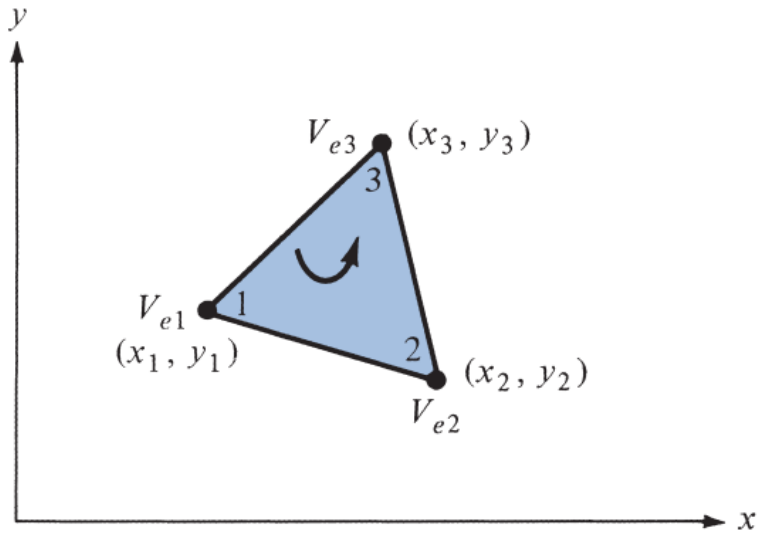

Figure 3.8: A typical triangular element [26].

$$\begin{bmatrix} V_{e1} \\ V_{e2} \\ V_{e3} \end{bmatrix} = \begin{bmatrix} 1 & x_1 & y_1 \\ 1 & x_2 & y_2 \\ 1 & x_3 & y_3 \end{bmatrix} \begin{bmatrix} a \\ b \\ c \end{bmatrix} \tag{3.39}$$

The coefficients a, b and c are then determined from these equations,

$$\begin{bmatrix} a \\ b \\ c \end{bmatrix} = \begin{bmatrix} 1 & x_1 & y_1 \\ 1 & x_2 & y_2 \\ 1 & x_3 & y_3 \end{bmatrix}^{-1} \begin{bmatrix} V_{e1} \\ V_{e2} \\ V_{e3} \end{bmatrix} \tag{3.40}$$

By using substitution, the equations for potential at various nodes become,

$$V_e = \sum_{i=1}^{3} \alpha_i(x, y) V_{ei} \tag{3.41}$$

Where,

$$\alpha_1 = \frac{1}{2A}[(x_2 y_3 - x_3 y_2) + (y_2 - y_3)x + (x_3 - x_2)y] \tag{3.42}$$

$$\alpha_2 = \frac{1}{2A}[(x_3 y_1 - x_1 y_3) + (y_3 - y_1)x + (x_1 - x_3)y] \tag{3.43}$$

$$\alpha_3 = \frac{1}{2A}[(x_1 y_2 - x_2 y_1) + (y_1 - y_2)x + (x_2 - x_1)y] \tag{3.44}$$

The area of element e,

$$A = \frac{1}{2}[(x_2 - x_1)(y_3 - y_1) - (x_3 - x_1)(y_2 - y_1)] \tag{3.45}$$

The energy per unit length W_e associated with element e is given by,

$$W_e = \frac{1}{2} \int \varepsilon |\nabla V_e|^2 dS \tag{3.46}$$

Where a charge free two dimensional solution region is assumed. However, substituting for ∇V_e, the energy per unit length becomes,

$$W_e = \frac{1}{2} \sum_{i=1}^{3} \sum_{j=1}^{3} \varepsilon V_{ei} \left[\int \nabla \alpha_i \cdot \nabla \alpha_j dS \right] V_{ej} \tag{3.47}$$

If we define the term in brackets as C_{ij}, then the matrix form of energy per unit length W_e becomes,

$$W_e = \frac{1}{2} \varepsilon V_e^T C^{(e)} V_e \tag{3.48}$$

Where,

$$V_e = \begin{bmatrix} V_{e1} \\ V_{e2} \\ V_{e3} \end{bmatrix} \tag{3.49}$$

and

$$C^{(e)} = \begin{bmatrix} C_{11}^{(e)} & C_{12}^{(e)} & C_{13}^{(e)} \\ C_{21}^{(e)} & C_{22}^{(e)} & C_{23}^{(e)} \\ C_{31}^{(e)} & C_{32}^{(e)} & C_{33}^{(e)} \end{bmatrix} \tag{3.50}$$

The matrix C is called the element coefficient matrix. The different elements are calculated as follows,

$$C_{11}^{(e)} = \frac{1}{4A}[(y_2 - y_3)^2 + (x_3 - x_2)^2] \tag{3.51}$$

$$C_{12}^{(e)} = \frac{1}{4A}[(y_2 - y_3)(y_3 - y_1) + (x_3 - x_2)(x_1 - x_3)] \tag{3.52}$$

$$C_{13}^{(e)} = \frac{1}{4A}[(y_2 - y_3)(y_1 - y_2) + (x_3 - x_2)(x_2 - x_1)] \tag{3.53}$$

$$C_{22}^{(e)} = \frac{1}{4A}[(y_3 - y_1)^2 + (x_1 - x_3)^2] \tag{3.54}$$

$$C_{23}^{(e)} = \frac{1}{4A}[(y_3 - y_1)(y_1 - y_2) + (x_1 - x_3)(x_2 - x_1)] \tag{3.55}$$

$$C_{33}^{(e)} = \frac{1}{4A}[(y_1 - y_2)^2 + (x_2 - x_1)^2] \tag{3.56}$$

Also,

$$C_{21}^{(e)} = C_{12}^{(e)}, \quad C_{31}^{(e)} = C_{13}^{(e)}, \quad C_{32}^{(e)} = C_{23}^{(e)} \tag{3.57}$$

3.4.3 Assembling of All Elements

The assembly of all elements is a crucial step in the Finite Element Method (FEM) process. This step combines the information obtained from individual finite elements to construct a global system of equations. This system is representative of the entire problem domain, considering every interaction between the finite elements. The energy associated with the assemblage of all elements in the mesh is,

$$W = \sum_{e=1}^{N} W_e = \frac{1}{2}\varepsilon V^T C V \tag{3.58}$$

Where,

$$V = \begin{bmatrix} V_1 \\ V_2 \\ V_3 \\ \vdots \\ V_n \end{bmatrix} \tag{3.59}$$

Let us consider the fig 3.9. Each of the elements has 3 nodes which can be represented by

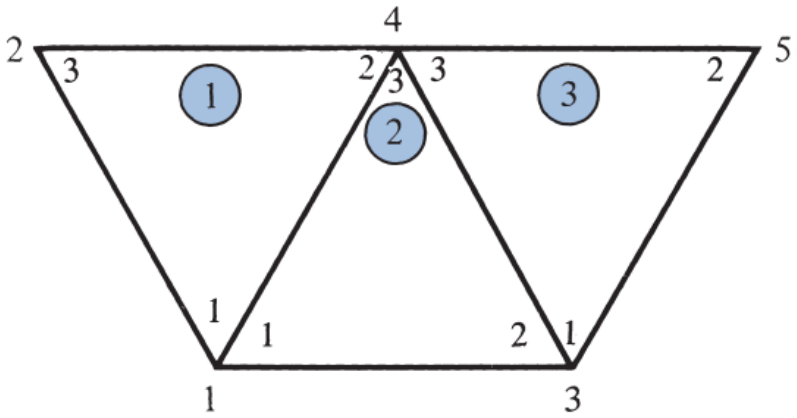

Figure 3.9: Assembly of three elements [26].

the global numbering and non-unique local numbering which must be done in counterclockwise sequence. However, global numbering describing the nodes must be unique. However, global numbering describing the nodes must be unique. Since there are 5 nodes the global coefficient matrix will have the following form,

$$C = \begin{bmatrix} C_{11} & C_{12} & C_{13} & C_{14} & C_{15} \\ C_{21} & C_{22} & C_{23} & C_{24} & C_{25} \\ C_{31} & C_{32} & C_{33} & C_{34} & C_{35} \\ C_{41} & C_{42} & C_{43} & C_{44} & C_{45} \\ C_{51} & C_{52} & C_{53} & C_{54} & C_{55} \end{bmatrix} \tag{3.60}$$

The diagonal elements of the global coefficient matrix are calculated such that each of the adjacent element's associated nodes as described by local numbering are added up. The rest of the elements of the global coefficient matrix are calculated such that the common line connecting the nodes determines which coefficients of each individual element are added. For example, for the global coefficient matrix element C_{14}, is assemblage of $C_{12}^{(1)}$ and $C_{13}^{(2)}$. Hence the global coefficient matrix becomes,

$$C = \begin{bmatrix} C_{11}^{(1)} + C_{11}^{(2)} & C_{13}^{(1)} & C_{12}^{(2)} & C_{12}^{(1)} + C_{13}^{(2)} & 0 \\ C_{31}^{(1)} & C_{33}^{(1)} & 0 & C_{32}^{(1)} & 0 \\ C_{21}^{(2)} & 0 & C_{22}^{(2)} + C_{11}^{(3)} & C_{23}^{(2)} + C_{13}^{(3)} & C_{12}^{(3)} \\ C_{21}^{(1)} + C_{31}^{(2)} & C_{23}^{(1)} & C_{32}^{(2)} + C_{31}^{(3)} & C_{22}^{(1)} + C_{33}^{(2)} + C_{33}^{(3)} & C_{32}^{(3)} \\ 0 & 0 & C_{21}^{(3)} & C_{23}^{(3)} & C_{22}^{(3)} \end{bmatrix} \tag{3.61}$$

3.4.4 Solving the Resulting Equations

The final step of finite element method is solving the algebraic equations derived from the derivative governing equations. Laplace's and Poisson's equations of EM are satisfied when total energy of the solution region is minimum. Hence,

$$\frac{\partial W}{\partial V_1} = \frac{\partial W}{\partial V_2} = \ldots = \frac{\partial W}{\partial V_n} \tag{3.62}$$

Therefore,

$$\frac{\partial W}{\partial V_i} = V_1 C_{i1} + V_2 C_{i2} + \ldots + V_n C_{in} = 0 \tag{3.63}$$

In general, from each of the node a set of equations is derived,

$$\sum_{i=1}^{n} V_i C_{ik} = 0 \tag{3.64}$$

Where n is the number of nodes in the mesh. Hence n simultaneous equations are derived from which the potential $[V]$ can be found out. One of the methods of solving this system of equations is the iteration method. At each of the free node, the potential can be calculated as,

$$V_k = -\frac{1}{C_{kk}} \sum_{i=1, i \neq k}^{n} V_i C_{ik} \tag{3.65}$$

This is then applied to all the nodes iteratively. At the 1st iteration the potential at the free nodes can be set to zero.

3.4.5 Scattering Analysis

In the case of open regions, the computational domain must be truncated properly. In our model, the incident field from the source is directly introduced on the scatterer. The vector

wave equation in such case is [116],

$$\nabla \times \left[\frac{1}{\mu}\nabla \times \mathbf{E}^{sc}(r,t)\right] + \epsilon\frac{\partial^2 \mathbf{E}^{sc}(r,t)}{\partial t^2} + \sigma\frac{\partial \mathbf{E}^{sc}(r,t)}{\partial t} = -\frac{\partial \mathbf{J}_{eq}(r,t)}{\partial t} \tag{3.66}$$

Where $\mathbf{J}_{eq}$ denotes the equivalent source by,

$$\frac{\partial \mathbf{J}_{eq}(r,t)}{\partial t} = \nabla \times \left[\frac{1}{\mu}\nabla \times \mathbf{E}^{inc}(r,t)\right] + \epsilon\frac{\partial^2 \mathbf{E}^{inc}(r,t)}{\partial t^2} + \sigma\frac{\partial \mathbf{E}^{inc}(r,t)}{\partial t} \tag{3.67}$$

3.4.6 Scattering Parameters

At high frequencies the voltage and current are not well defined hence S-parameters are used to analyze the state of the field. S parameters are a complex set of quantities which can be used to calculate the field at various ports. At port i with excitation,

$$E_{\text{ec}} = E_i + \sum_{j=1} S_{ji}E_j \tag{3.68}$$

At ports with no excitation,

$$E_{\text{ec}} = \sum_{j=1} S_{ji}E_j \tag{3.69}$$

$$S_{11} = \frac{\int_{\text{port1}}(\mathbf{E}_{ec} - \mathbf{E}_1)\cdot\mathbf{E}_1 dA_1}{\int_{\text{port1}}\mathbf{E}_1\cdot\mathbf{E}_1^* dA_1} \tag{3.70}$$

$$S_{21} = \frac{\int_{\text{port2}}(\mathbf{E}_{ec} - \mathbf{E}_2)\cdot\mathbf{E}_2 dA_2}{\int_{\text{port1}}\mathbf{E}_2\cdot\mathbf{E}_2^* dA_2} \tag{3.71}$$

$$S_{31} = \frac{\int_{\text{port3}}(\mathbf{E}_{ec} - \mathbf{E}_3)\cdot\mathbf{E}_1 dA_3}{\int_{\text{port3}}\mathbf{E}_3\cdot\mathbf{E}_3^* dA_3} \tag{3.72}$$

Hence S parameters of an N port device can be expressed as,

$$\begin{bmatrix} S_{11} & \cdots & S_{1n} \\ \vdots & \ddots & \vdots \\ S_{N1} & \cdots & S_{NN} \end{bmatrix} \tag{3.73}$$

3.4.7 Miscellaneous Terms

Port Analysis: Ports are where inputs and outputs are calculated. The power flow at the ports can be calculated by Poynting vector,

$$\mathbf{S}_{avg} = \frac{1}{2}\text{Re}(\mathbf{E} \times \mathbf{H}^*) \tag{3.74}$$

Mode Analysis: In this analysis the lowest fundamental mode that can satisfy the field conditions within the waveguide is calculated. Via this analysis the propagation constant is solved which is a complex quantity,

$$k = k' + jk'' \tag{3.75}$$

The real part denotes the propagation constant while the imaginary part denotes the damping along the propagation.

3.5 Performance Parameters

There are various performance parameters that can quantify the effectiveness of our nanosensor. These parameters provide us with a thorough understanding of the sensor's performance under various conditions and serve as benchmarks for comparing our sensor to others. We will delve into four of these key parameters: Sensitivity, Figure of Merit (FOM), Quality Factor (Q), and Detection Limit.

3.5.1 Sensitivity (S)

Sensitivity is a measure of how the sensor's output changes in response to a change in the input (the analyte concentration in our case). In the context of our refractive index sensor, it is defined as the change in the resonance wavelength (depending on the interrogation technique) per unit change in the refractive index.

$$S = \frac{\Delta\lambda}{\Delta\eta}$$

Where, $\Delta\lambda$ is the change in wavelength and $\Delta\eta$ is the change in refractive index.

Higher sensitivity allows for more accurate detection of smaller changes in the analyte concentration. We determine the sensor's sensitivity via using simulation in Comsol Multi-

physics by changing the refractive index and recording the corresponding change in the sensor's output.

3.5.2 Figure of Merit (FOM)

The FOM is a measure of the sensor's overall performance, considering both its sensitivity and its resolution. In plasmonic sensors, the FOM is usually defined as the sensitivity divided by the full width at half maximum (FWHM) of the resonance dip,

$$FOM = \frac{S}{FWHM}$$

The FOM provides an overall measure of sensor performance, with higher FOM indicating better performance. Like sensitivity, the FOM is determined experimentally. For calculating FWHM the average of maximum and minimum transmittance around the point of interest is taken. Then the difference between the two wavelength that intersect with the average transmittance line is calculated as FWHM.

3.5.3 Quality Factor (Q)

The Quality Factor of a resonator is a measure of how sharp the peak or the valley is. It is defined as following,

$$Q = \frac{\lambda_{resonant}}{FWHM}$$

It is used for measuring filtering performance. A higher Q factor means better resolution in detecting changes in the refractive index.

3.5.4 Detection Limit (DL)

The detection limit of the sensor is the smallest change in the refractive index that the sensor can reliably detect. It is calculated as,

$$DL = \frac{\Delta\lambda_{min}}{S}$$

A lower detection limit is desirable as it means the sensor can detect smaller changes in refractive index.

3.6 Re-simulation of existing sensor

In the course of our research, we attempted to establish the validity and dependability of our computational model by comparing our findings to those outlined in a previously published paper. This endeavor required meticulously recreating the simulations described in the aforementioned paper and matching our simulation setup parameters to those used in the original study. We have re-simulated Mahmud et al. [27] triangular disk resonator shown in fig 3.10.

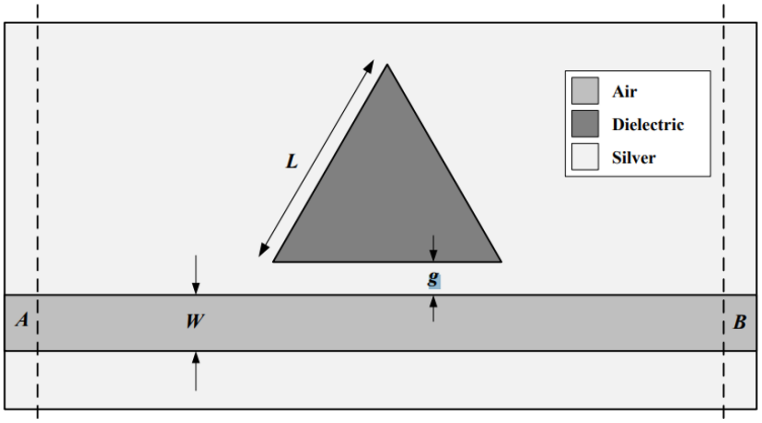

Figure 3.10: Structure that has been re-simulated [27].

The nanostructure's transmittance response was a crucial comparing factor. In the context of our investigation, transmittance refers to the proportion of incident light that passes through the structure. The precision of our modeling and simulation processes is determined by comparing the transmittance spectra. Our resimulation produced a transmittance curve that

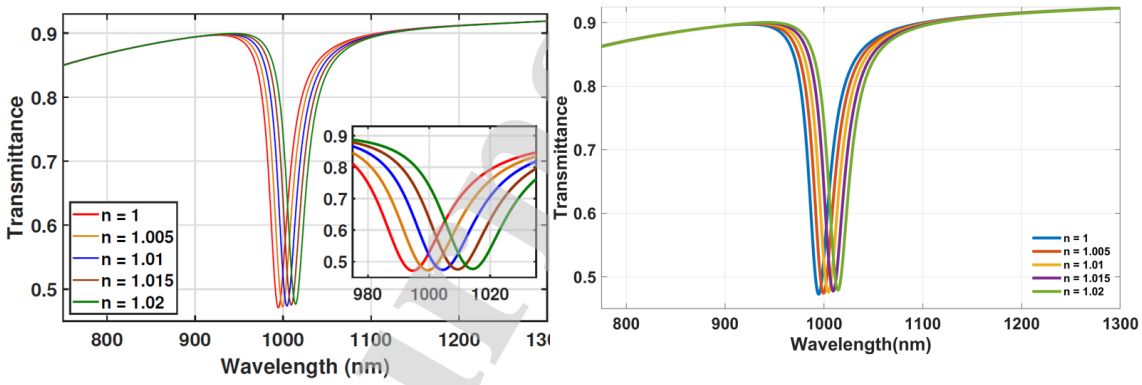

(a) Paper result **(b) Our result**

Figure 3.11: Comparison of transmittance spectrum [27].

closely matched the one presented in the paper depicted in fig 3.11, thereby reinforcing our

faith in the accuracy of our model. This agreement demonstrates the robustness of our computational methods and highlights the dependability of our research. In addition, it allows us to build upon these foundations in future investigations.

Chapter 4

Numerical Analysis of On-Chip RI sensor

4.1 Sensor Design and Formulation

The proposed structure has been illustrated in fig 4.1. Nano dots have been embedded in the round-edged-hexagonal resonator, which has been coupled to two straight waveguides implanted with nanodots. Nanodots help in the confinement of SPPs and they increase the total electrical energy [117]. Due to gold nanodots, enhanced coupling can be observed due to gap plasmon resonance (GPR), which improves the device's sensing ability [77]. Hexagon has six bends, and bending losses are the leading source of losses in bends [118]. So, in order to decrease the bending losses, rounded edges of 40 nm has been used.

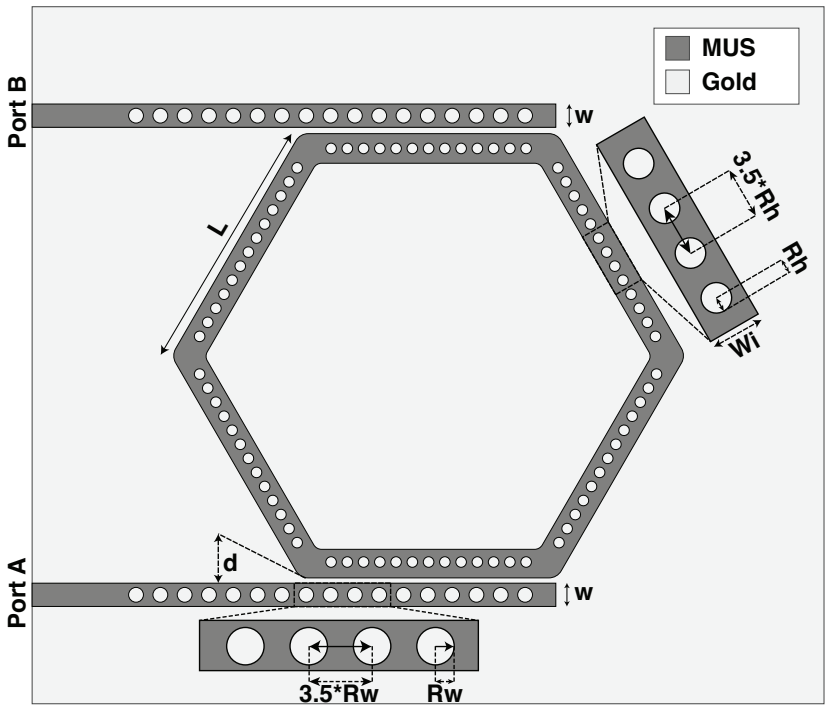

Figure 4.1: Diagram of the suggested design

The circumradius of a circle (R) that traverses the six vertices of a hexagon is equal to the length of the hexagon's side (L). The MIM structure consists of gold due to resistance to oxidation, and the material under sensing (MUS) is used to fill the two straight waveguides and the resonator. The analyte can be sent to the cavity by electro-spraying from a nanofluidic capillary [119] or a nano-filling technique based on capillarity attraction [120]. Port A is the input port where SPPs are excited, and Port B is the output port. The proposed sensor can be fabricated using electron-beam lithography (EBL), focused ion beam (FIB) lithography, nanoimprint lithography (NIL), or any other fabrication technology providing high resolution. Among them, NIL technology offers cost-effective mass production with high throughput. Unlike the conventional light-exposure-based lithography processes, the nanoimprint lithography process transfers the desired pattern on the resist mechanically. As a result, it overcomes the limitations caused by light diffraction or beam scattering and yields high resolution easily [121].

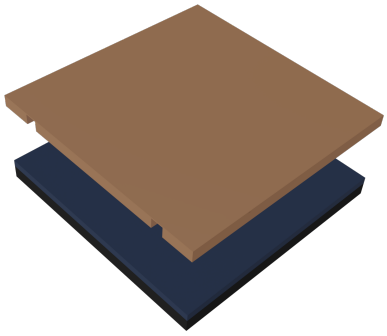

Figure 4.2: UV transparent flexible stamp is prepared from a master mold, and the substrate is coated with UV-curable resist.

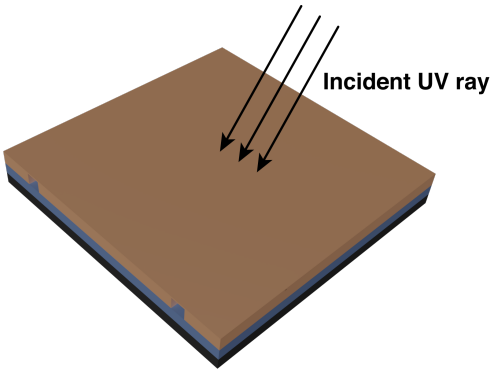

Figure 4.3: The stamp is pressed on the resist, and UV light is shone on the sample to harden the liquid resist.

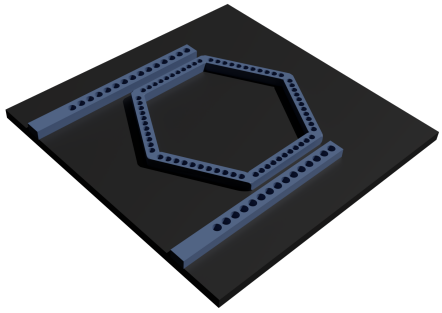

Figure 4.4: The stamp is removed, and RIE removes the residual part of the resist

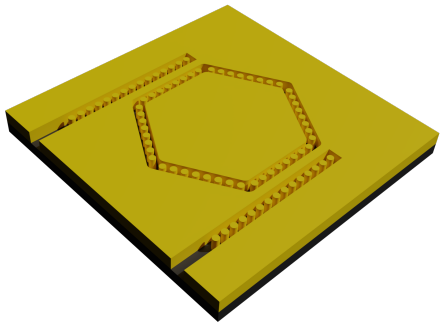

Figure 4.5: Gold is deposited on the structure, and the resist is lifted off.

Traditional NIL, known as thermal assist NIL (T-NIL), uses a hard mold to imprint the pattern onto a thin layer of thermoplastic resist at high temperature and pressure [122]. One upgraded version of NIL, known as soft UV nanoimprint lithography, offers fabrication on a full wafer scale in one step at room temperature and low pressure [123]. Therefore, this upgraded soft UV NIL technology becomes cheaper and more efficient, making it applicable to our proposed sensor. This process has been illustrated in fig 4.2,4.3,4.4,4.2. The Soft UV-NIL process uses a UV transparent flexible stamp made from a master mold. This stamp transfers the desired pattern on a UV-curable resist which is liquid at room temperature. First, the resist is coated on the substrate. Then the stamp is pressed on the resist maintaining low pressure and room temperature. After that, the sample is exposed to a UV light source. Typically a dose of around $10^5\ J/m^2$ is applied [124], which results in a photochemical reaction inside the resist and hardens it. After UV light exposure, the stamp is removed, leaving the resist imprinted with the desired pattern. Next, the Residual layer of resist is removed by etching using Reactive Ion Etching (RIE). After that, a layer of gold is deposited on the substrate using electron beam evaporation. Finally, the resist is eliminated by a lift-off process using ultrasonic agitation in acetone [125], leaving behind the desired gold structure on top of the substrate.

For the purpose of modeling the sensor, COMSOL Multiphysics has been used, which employed the Finite Element Method (FEM) by meshing (triangular) the whole structure. Scattering boundary conditions have been included at the edges to prevent back reflection of

the emitted wave from the computational domain's exterior boundary. Danaie et al. [126] demonstrated that the performance parameters of the device in 3D will be highly comparable to those achieved in 2D at any height greater than 800 nm. Thus, a 2D simulation has been carried out for faster computational time. This type of plasmonic structure has also been constructed experimentally [127–129].

4.2 Simulation and results

The MUS has been loaded with dielectric material with n = 1.3, as most of the bio and chemical analytes have their refractive index close to this value. The resonance is heavily affected by both the change in the refractive index of the material being sensed and the geometry of the sensor. Because the size of SPP-based optical devices is on the nanometer scale, it is challenging to build these devices. As a result, the simulation approach may optimize the device structure while simultaneously lowering the cost of the experiments.

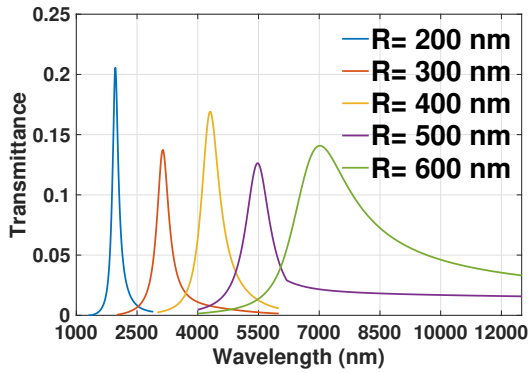

(a) Transmittance

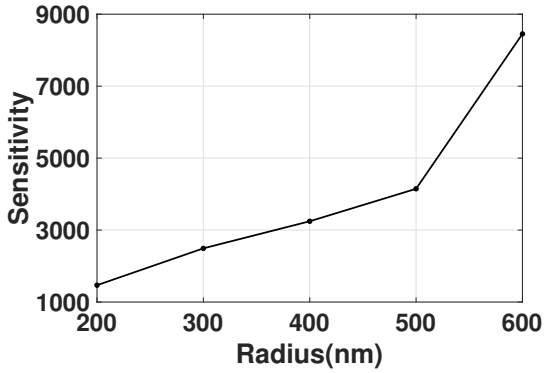

(b) Sensitivity

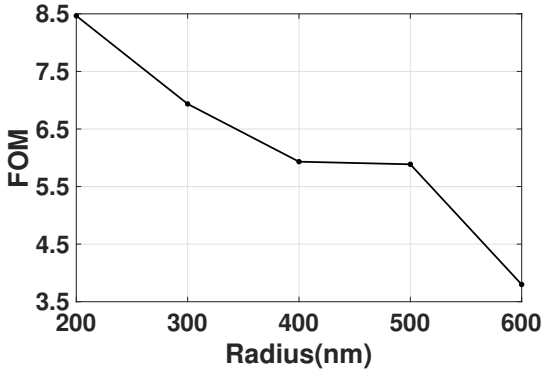

(c) FOM

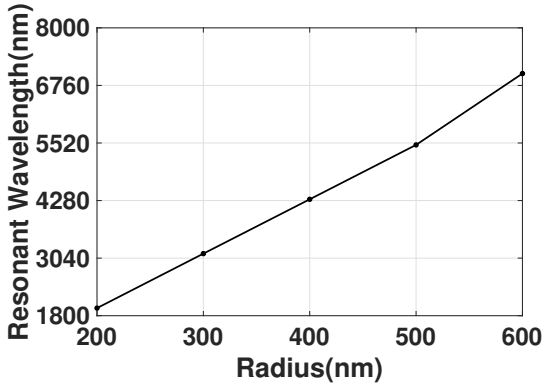

(d) Resonant Wavelength

Figure 4.6: (a) Transmission spectrum for different radius and (b), (c), (d) change in Sensitivity, FOM, and resonant wavelength as radius is varied

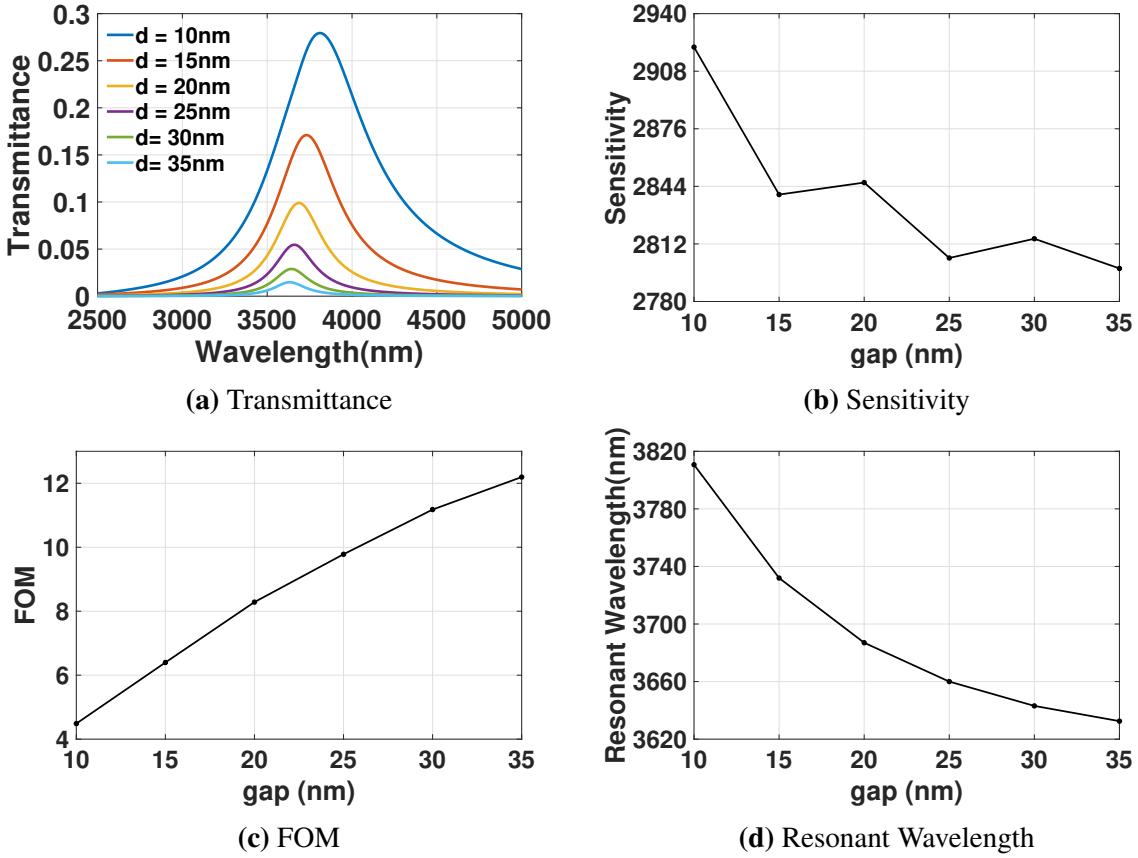

(a) Transmittance **(b)** Sensitivity

(c) FOM **(d)** Resonant Wavelength

Figure 4.7: (a) Transmission vs wavelength and (b), (c), (d) Sensitivity, FOM, and resonant wavelength as d is varied.

Initially, the structure is simulated without any nanodots. The initial parameters are given as follows, $R = 350$ nm, $wi = 45$ nm, $d = 15$ nm, $w = 50$ nm, $bend = 40$ nm. The hexagonal resonator's radius has been varied from 200 nm to 600 nm with a 100 nm step size. The transmittance, sensitivity, and FOM change with radius variation has been illustrated in fig 4.6. From equation 3.35, it can be seen that as R is increased, there is a redshift in the resonant wavelength. From fig 4.6d, we can see that as R ($\mathrm{R} = \mathrm{L_D}$) is increased, the resonant wavelength increases verifying our simulation result with the theoretical analysis. The sensitivity increases sharply from 500 nm to 600 nm, and FOM also decreases sharply, as there is usually a tradeoff between sensitivity and FOM. For achieving high sensitivity, $R = 550$ nm has been chosen as the final parameter. Next, the gap (d) between the resonator and the input and output waveguides is varied from 10 nm to 35 nm with a 5 nm step size. All the other parameters are kept the same. The transmission spectrum and performance parameters change has been given in fig 4.7. SPPs decay evanescently, so as the gap is deceased more of the SPP is coupled to the resonator, increasing the transmittance. From fig 4.7a, we can see that as the gap has decreased, the transmittance also increases, which verifies our theoretical analysis. The gap for the final structure is chosen as 15 nm for high sensitivity and better coupling of SPPs. To investigate the impact on the performance of the

width of the resonator (Wi), Wi has been varied from 20 nm to 60 nm with a 10 nm step size keeping all other parameters constant. The transmittance and performance indicators have been illustrated in fig 4.8. As the width is decreased SPPs confinement is increased, increasing the sensitivity. For R and d, the priority was sensitivity. In this case, FOM has been given priority, and the final value for Wi has been chosen as $Wi = 45$ nm. Then building the structure with these final parameter values, nanodots were incorporated in both the straight waveguide and hexagonal resonator. 17 dots with $Rw = 15$ nm radius and $3.5 * Rw$ distance between the dots have been incorporated in the straight waveguides. After that, 3, 5, 9, and 13 dots in each arm (N_L) with radius, $Rh = 10$ nm and $3.5 * Rh$ distance between them has been incorporated gradually, and the sensitivity variation is given in fig 4.9. We previously stated that nanodots help in SPPs confinement and increase the electric energy. For this reason, the sensitivity rises as the number of nanodots increases. $N_L = 13$ has been chosen for this reason.

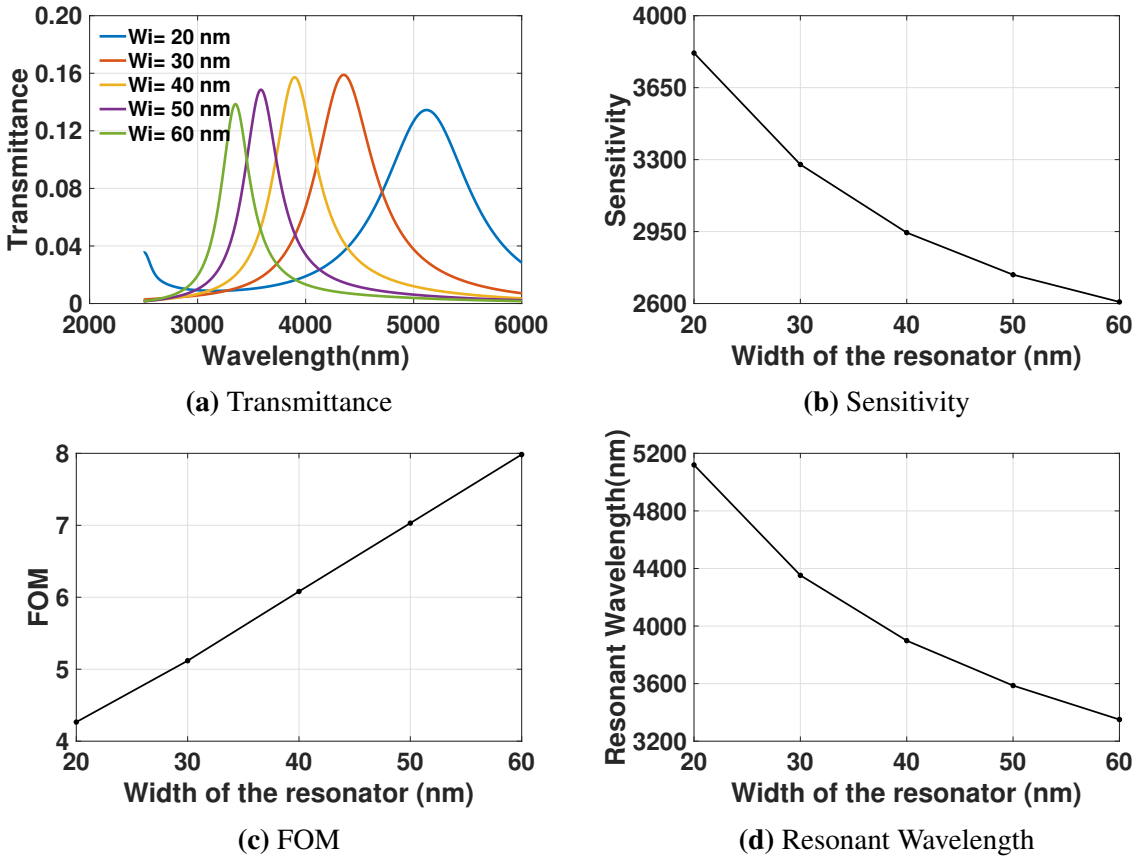

(a) Transmittance

(b) Sensitivity

(c) FOM

(d) Resonant Wavelength

Figure 4.8: (a) Transmission vs wavelength and (b), (c), (d) Sensitivity, FOM, and resonant wavelength change as the width of the hexagonal resonator is varied.

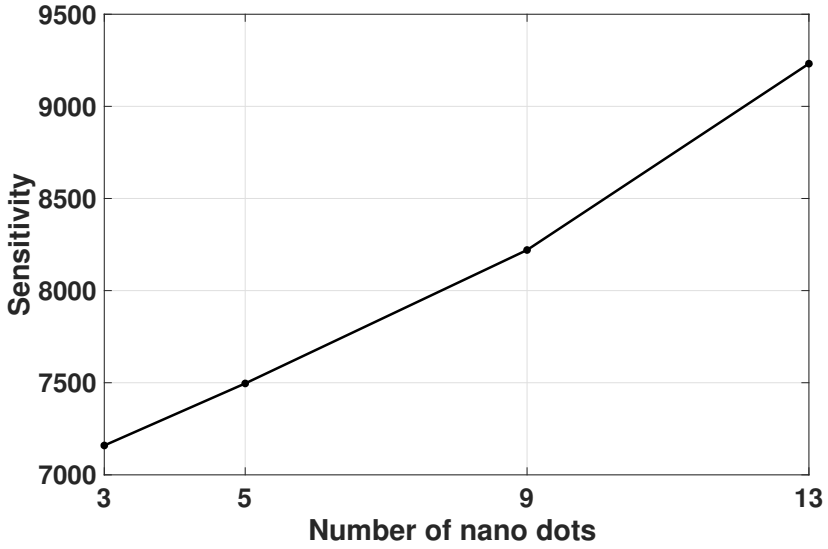

Figure 4.9: Number of nanodots increasing sensitivity as electric field is confined more

Table 4.1: Geometric Parameters after optimization.

Parameters	Representation	Value
Radius	R	550 nm
Gap	d	15 nm
Width of resonator	Wi	45 nm
Nano dots in each arm	N_L	13
Radius of nano dots	Rh	10 nm
Straight waveguide width	w	50 nm

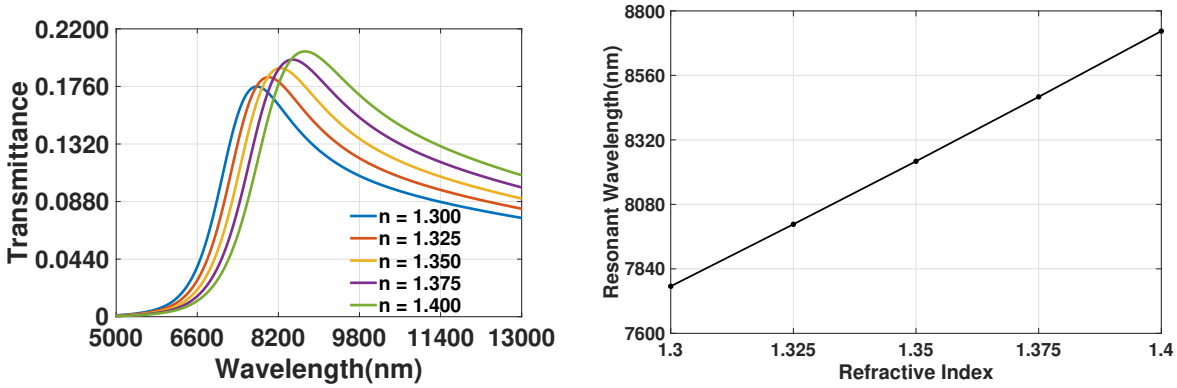

(a) Transmittance **(b)** Sensitivity

Figure 4.10: (a) Transmittance spectrum for $n = 1.3$ to $n = 1.4$ with 0.025 step size (b) Refractive index vs Resonant wavelength

Table 4.1 provides the values for the final parameters considering optimal performance. The shift in the resonant wavelength that occurs in response to a shift in the refractive index is seen in fig 4.10. We can see (fig 4.10b) that there is a linear relationship between the refractive index and the resonant wavelength verifying our FEM simulation. The max sensitivity, FOM, and Sensing Resolution for the optimal parameters are 9231.7, 5 ,$1.083 * 10^{-7}$ for the

refractive index 1.3 and 1.325. In Transverse Magnetic mode, $H_x = 0$, $H_y = 0$, and $E_z = 0$. The Hz field and the electric field distribution is given in figure 8 a and b. As light is restricted on a subwavelength scale, the electric field is enhanced, and nanodots help enhance the electric field even more, which is evident from fig 4.11b.

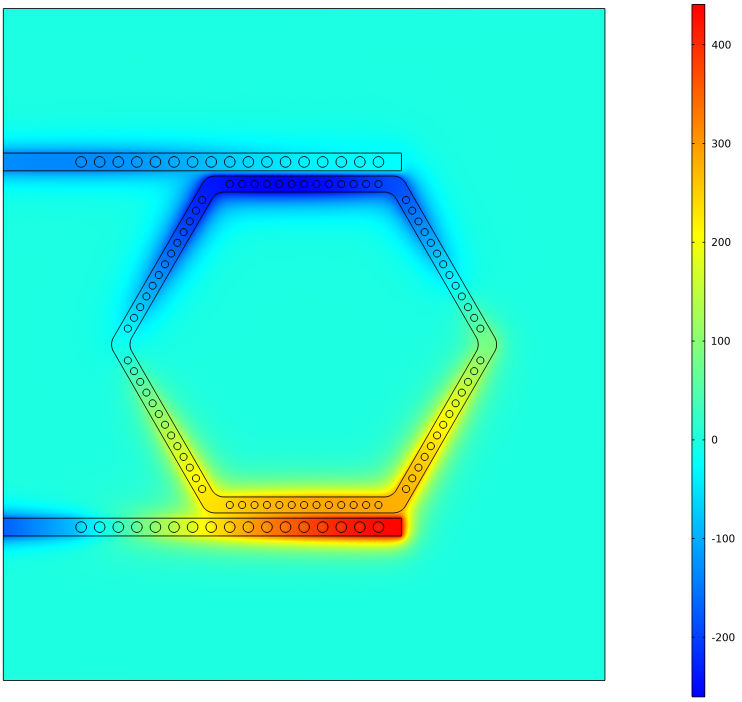

(a) Hz (A/m) component of magnetic field

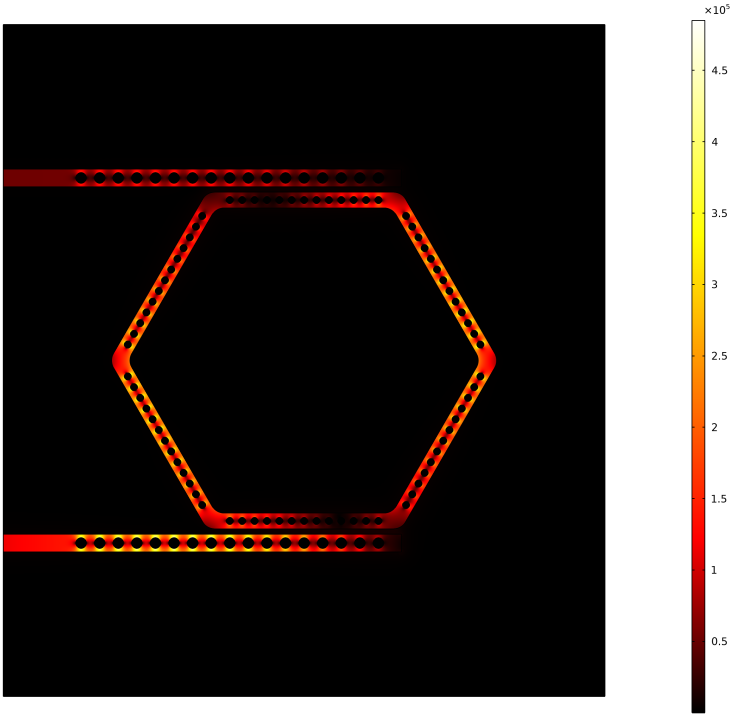

(b) Electric field distribution

Figure 4.11: Electric and magnetic field distribution at resonant wavelength for $n = 1.3$

4.3 Application

4.3.1 Salinity measurement

The amount of salt in ocean water substantially affects the capacity of marine plants and animals to survive and spread. Variations in the worldwide distribution of fresh and salty waters in the ocean are occurring all over the world, and these variations indicate possible linkages to global warming and potential alterations in the hydrologic cycle of the Earth [130]. Salinity measurement will aid scientists in diagnosing rates of surface freshwater fluxes, freshwater transport, and local ocean mixing [130]. That is why this sensor has been evaluated for the measurement of salinity in seawater. The refractive index of seawater is related to Salinity by the following empirical equation [131],

$$n(S,T,\lambda) = n_0 + (n_1 + n_2 T + n_3 T^2)S + n_4 T^2 + \frac{n_5 + n_6 S + n_7 T}{\lambda} + \frac{n_8}{\lambda^2} + \frac{n_9}{\lambda^3} \tag{4.1}$$

,where the coefficient values of n_0 to n_8 were obtained from literature [131], S is the salinity in ppt (parts per thousand), T is the temperature taken as 25°C and λ is the wavelength.

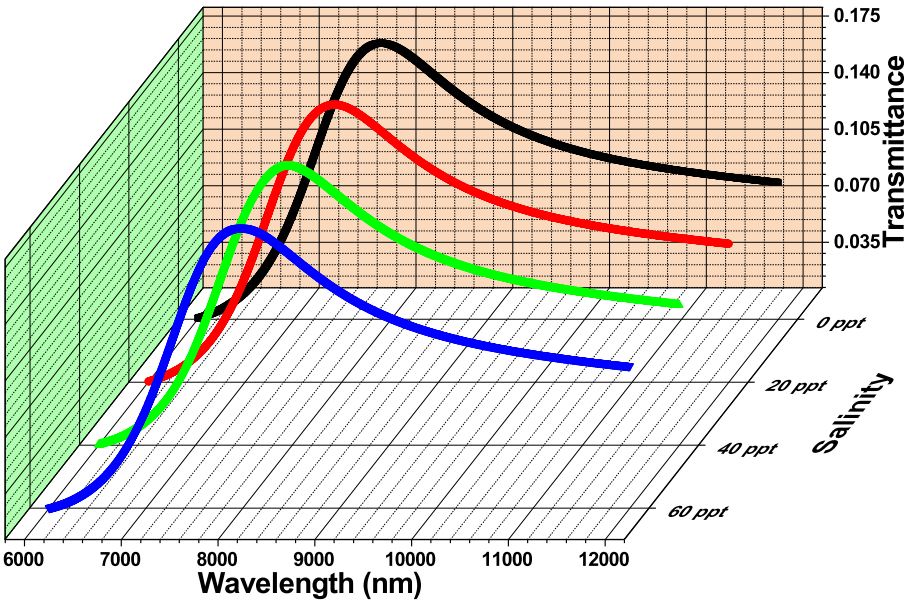

Figure 4.12: Transmittance vs wavelength for 0 ppt to 60 ppt salinity levels.

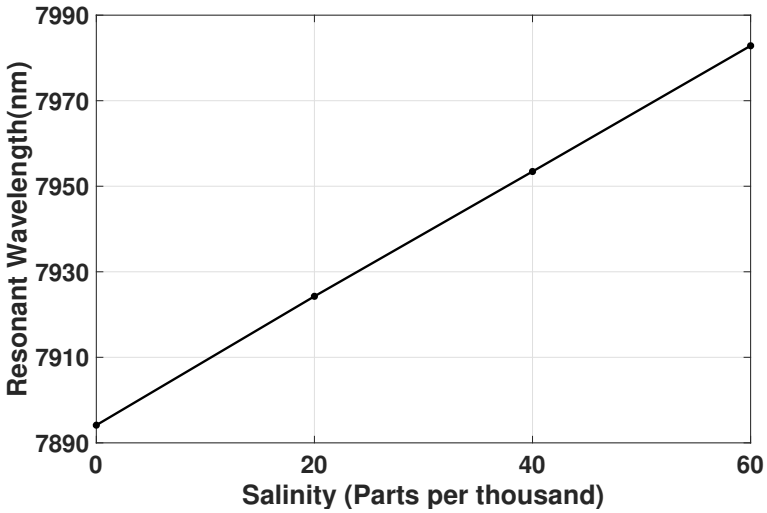

Figure 4.13: Resonant wavelength vs Salinity.

The transmittance for different salinity levels and resonant wavelength vs salinity has been plotted in fig 4.12 and fig 4.13. The sensor achieves 1476.6 nm/ppm sensitivity ($\Delta\lambda_{res}/\Delta S$) for salinity measurement.

4.3.2 Cell protein concentration measurement

Due to the fact that the cytoplasm makes up the bulk of a cell and proteins make up the most considerable proportion of cell solids in the cytoplasm, a single cell can be thought of as a container of protein solution. The turnover of proteins necessary to maintain protein levels consumes a considerable proportion of overall ATP turnover; within the cell, the cell protein may impede diffusion and solubility [132]. That is why studying cell protein concentration in nanomedicine applications is essential. Micropipette isolation, Laser capture microdissection, Capillary-based technology, and Microfluidic platforms can be used to extract cells [133]. The effective cell refractive index is related linearly to the protein content of the cell by the following equation [134]:

$$n - n_m = \alpha C \tag{4.2}$$

,where C is the grams of solute per 100mL, alpha is specific refraction increment (0.001845) and n_m is the refractive index of water.

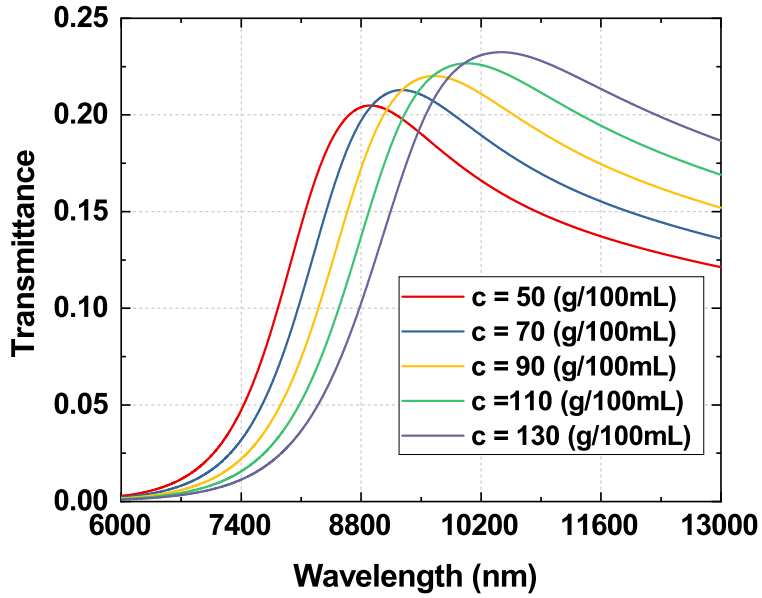

Figure 4.14: Transmission spectra for different cell protein concentration

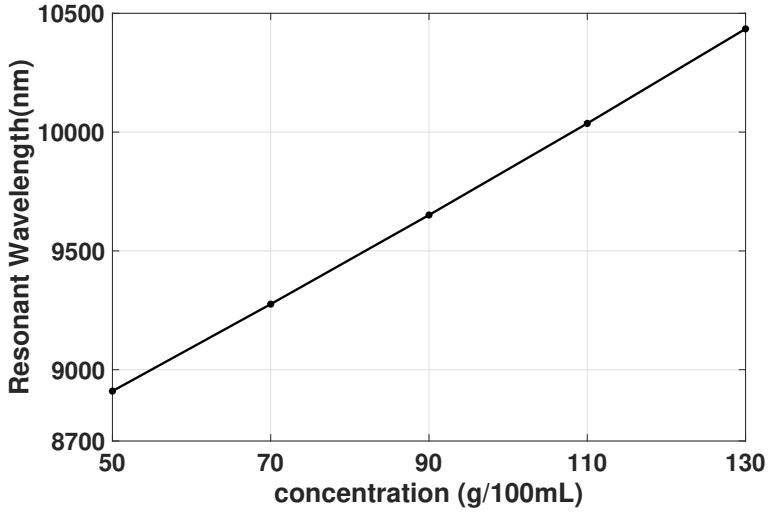

Figure 4.15: Resonant wavelength vs cell protein concentration

The transmittance for different concentrations has been plotted in fig 4.14. From the resonant wavelength vs concentration graph (fig 4.15), we see a linear relationship and concentration sensitivity ($\Delta\lambda_{res}/\Delta C$), which is equal to 19.05 nm/g/100mL.

4.3.3 BSA concentration measurement

Due to its remarkable structural similarity to human serum albumin (HSA), bovine serum albumin (BSA) has been extensively studied as a model protein in a wide range of scientific fields and therefore, determining BSA concentration in the biomedical, pharmaceutical, and

food sectors is essential [135]. BSA is used in the growth of cells in culture [136], in vitro anticancer therapy using atorvastatin calcium-loaded BSA (ATV-BSA) nanoparticles [137], so it is vital to measure BSA concentration. BSA can be extracted with 100% extraction efficiencies up to high protein concentration by aqueous biphasic systems of phosphonium- and ammonium-based ionic liquids [138]. Different techniques are used to assess protein concentration, including the Biuret method, Lowry method, Bradford method, and Bromocresol Green method, although these methods have numerous limitations, such as limited sensitivity, sample treatment, inadequate detection limit, restricted dynamic range [135]. That is why we propose this label-free detection system. The relation between the refractive index and concentration is taken from Chan-Yuan Tan et al. [139]. The transmittance vs BSA concentration is given in fig 4.16. From fig 4.17 we can get the following relationship by using curve fitting technique:

$$C\%(kg/kg) = -0.544 \times \lambda_{res}^2 + 5.998 \times \lambda_{res} + 7.935 \tag{4.3}$$

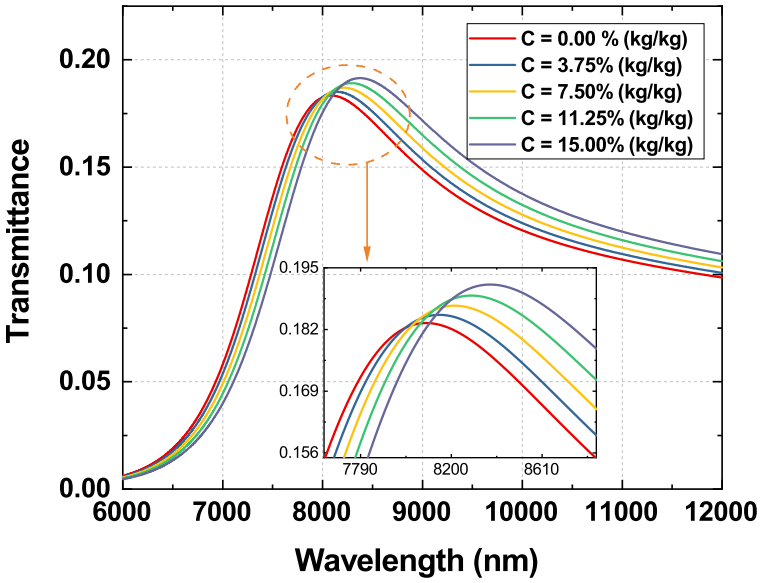

Figure 4.16: Transmission spectra for different BSA protein concentration %(kg/kg).

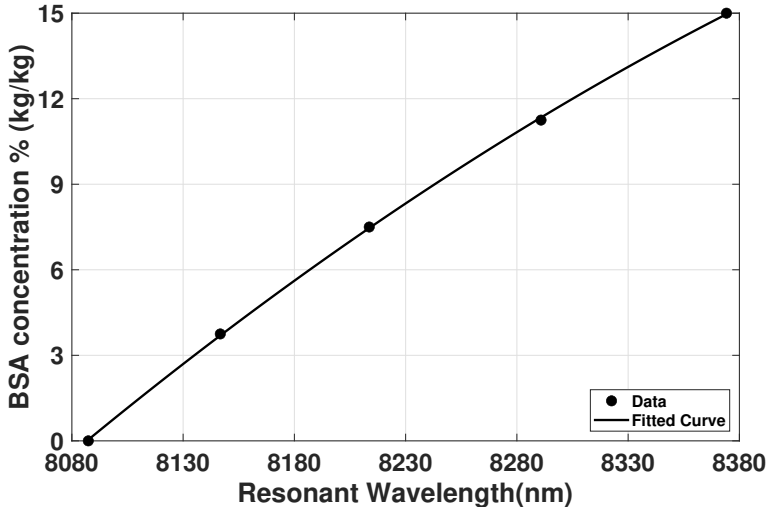

Figure 4.17: BSA concentration vs resonant wavelength

,where λ_{res} (nm) is normalized by mean (8223) and standard deviation(113.8). So, after seeing the resonant wavelength in an Optical spectrum analyzer, using this equation, one can find out the concentration of BSA.

4.3.4 Temperature measurement

Temperature sensitivity, which is a crucial characteristic of optical devices owing to the thermo-optic phenomena, becomes one of the potential factors affecting the performance of Multiprocessor systems-on-chips (MPSoCs), which can be safeguarded by a RI-based temperature sensor [63]. This equation illustrates the link between toluene's RI and its temperature [140],

$$n_{Toluene(\lambda)} = 1.474775 + \frac{6990.31}{\lambda^2} + \frac{2.1776 \times 10^8}{\lambda^4} - 5.273 \times 10^{-4}(T - T_0) \tag{4.4}$$

The temperature, T, is increased from 0°C to 80°C, with a step size of 20°C for toluene. The assumed ambient temperature, T_0, is taken as 20 °C. The transmission profile is given in fig 4.18, and the resonant wavelength vs temperature is given in fig 4.19. Temperature sensitivity is defined as $\Delta\lambda_{res}/\Delta T$. The temperature sensitivity 5.16 nm/°C has been achieved. The advantage of this type of temperature sensor is that they are electromagnetic interference-free.

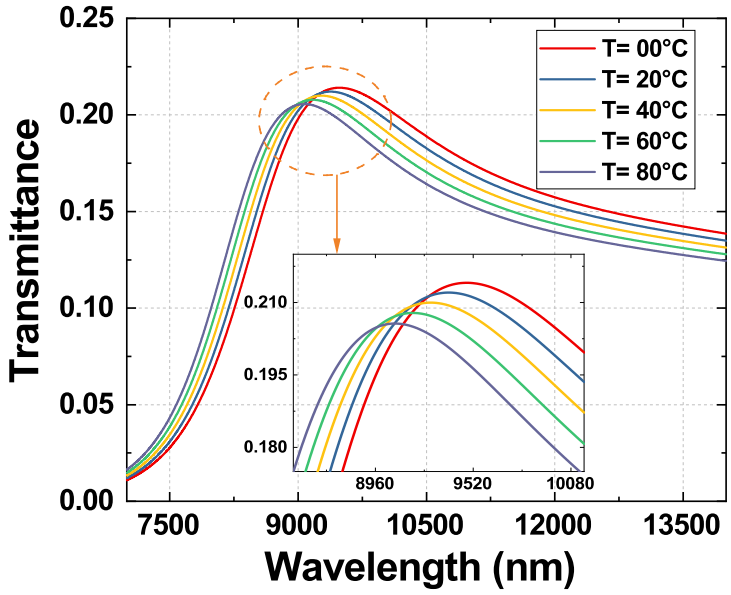

Figure 4.18: Transmittance for different temperature of toluene.

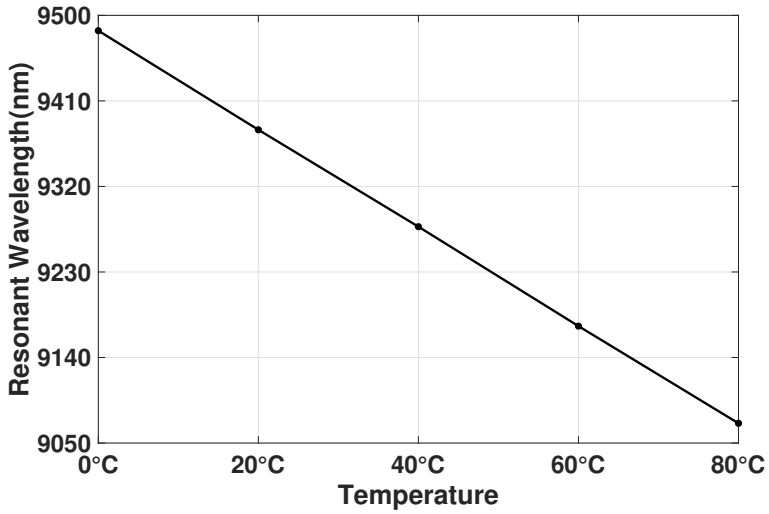

Figure 4.19: Resonant wavelength vs temperature of toluene

4.3.5 Tissue classification

At last, this sensor has been employed for the classification of various tissue types like the ileum, kidney, colorectal, and adrenal gland tissue. The refractive index of the tissues is related by the Cauchy equation:

$$n = A + \frac{B}{\lambda^2} + \frac{C}{\lambda^4} \tag{4.5}$$

and the Cauchy coefficients (A, B and C) for the aforementioned tissue types are obtained from literature [140, 141]. The transmission profile and resonant wavelength vs refractive index is given in fig 4.20 and fig 4.21 for different tissue types.

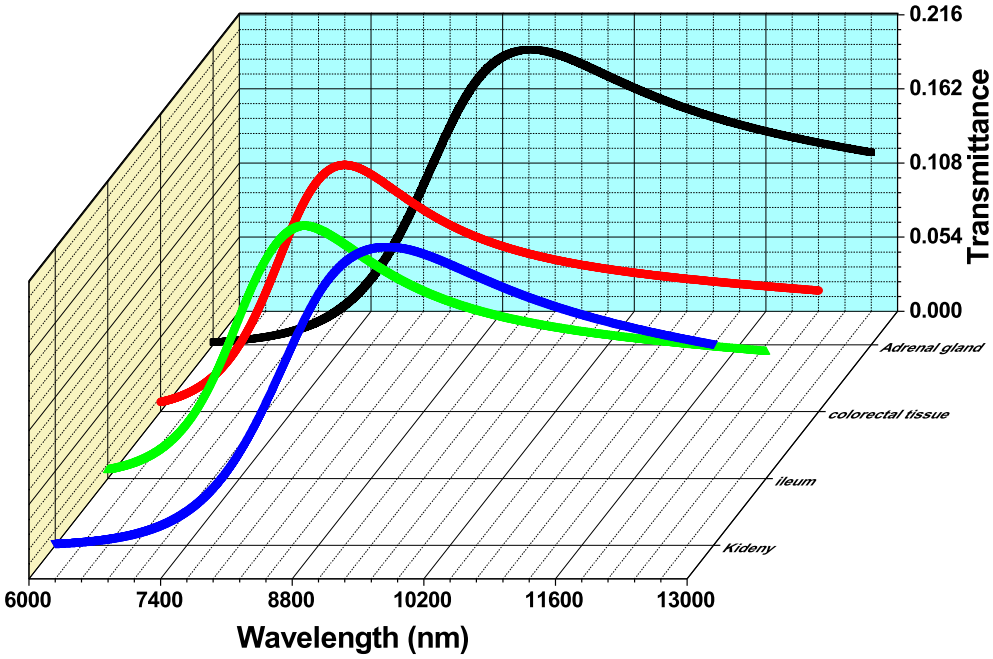

Figure 4.20: Transmittance profile for different types of tissue

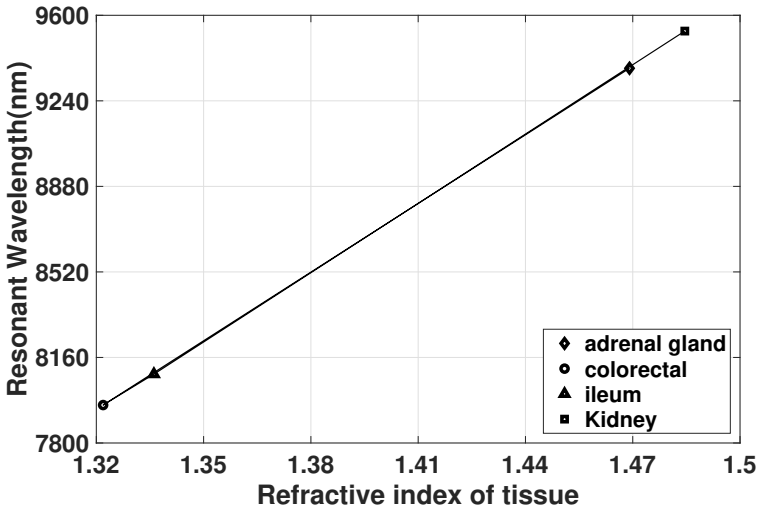

Figure 4.21: Refractive index vs resonant wavelength for the tissue types

Malignant tissue like Adenocarcinoma, Tubulovillous adenoma deviate from the expected refractive index [140], which will cause a change in λ_{res}, thus giving us the possibility of detection of malignant tissue if the tissue type is known beforehand.

4.3.6 Comparison

A comparison has been made between articles published in various journals in Table 4.2. It is evident that the majority of publications exhibit oxidation issues. In addition, many of them use the erroneous Drude model. This sensor adds a new dimension to the literature in terms of novel sensing applications.

Table 4.2: Comparative analysis of sensitivity and application with current literature of MIM-based sensors.

Reference	Sensitivity (nm/RIU)	Material and model	Oxidation problem	Application
[65]	900	Au (Drude-Lorentz)	Absent	Tuberculosis in Blood Plasma
[142]	1295	Ag (Drude)	Present	None
[143]	1400	Au (Drude)	Absent	Different ambient RI sensing
[35]	1556	Ag (Drude)	Present	Temperature sensing, Blood Group Sensing
[144]	2000	Ag (Drude)	Present	None
[77]	2473	Ag (Drude)	Present	Glucose concentration detection
[145]	3172	Ag (Drude-Lorentz)	Present	Blood Group Detection
[146]	6000	Ag (Drude)	Present	None
[63]	6227.6	Au (Drude-Lorentz)	Absent	Temperature measurement
[110]	7564	Ag (Drude-Lorentz)	Present	Blood Electrolytes, Glucose and Temperature
This work	9231.7	Au (Drude-Lorentz)	Absent	Salinity measurement, Cell protein and BSA concentration, Tissue classification, Temperature measurement

Chapter 5

Conclusions

The study of plasmonics, a subfield of nanophotonics, has enabled the generation and manipulation of electromagnetic waves beyond the diffraction limit. The use of localised electromagnetic waves in nanoscale integrated circuits was previously hampered by the diffraction limit, which has now been circumvented by these capabilities. In this paper, we explored Surface Plasmon Polaritons (SPPs) as an innovative solution. SPPs are a guided electromagnetic wave that propagates along the metal-dielectric interface, offering improved control and applicability for the creation of various nanoscale devices. Examining the significant advances in the field of plasmonic sensors, with a focus on the prevalent Metal-Insulator-Metal (MIM) structures, which have demonstrated strong electromagnetic wave confinement despite their higher losses compared to Insulator-Metal-Insulator (IMI) structures. We highlighted the promise of the mid-infrared spectral range for advancements in optical sensor technology, particularly in the domain of Lab-on-a-chip (LOC) applications, where RI sensors offer numerous advantages. Due to the low cost, portability, small footprint, small sample amount, and label-free detection capabilities of plasmonic refractive index sensors, it is crucial to create new sensing applications for these sensors while considering the fabrication challenge and silver oxidation issue. The limitations of the Drude model for material modelling, the oxidation problem of silver, the lack of comprehensive fabrication techniques, and the need for more diverse applications were identified as deficiencies in the current body of research. In response to these limitations, we proposed a solution: a gold-based hexagonal MIM refractive index sensor with rounded edges incorporating nano dots. This proposed sensor provides a wide range of previously unexplored applications. Gold, an oxidation-free plasmonic alternative to silver, was used to construct the hexagonal sensor with nanorods implanted for electric field amplification. The geometry has been tuned to achieve 9231.7 nm/RIU maximum sensitivity. The study has found that the sensitivity and resonance rely heavily on the structural design and number of nanorods. In addition, the gap between the resonator and straight waveguide substantially affects coupling. An inexpensive Soft UV-NIL technique

has been illustrated to ease the fabrication of the proposed sensor with high throughput at room temperature. The sensor has been evaluated in various sensing applications, including salinity measurement with a sensitivity of 1476.6 nm/ppm, cell protein concentration measurement with a sensitivity of 19.05nm/g/100mL, BSA concentration measurement, tissue classification, and temperature measurement using toluene with a sensitivity of 5.8nm/°C. A polynomial equation that links resonant wavelength from the spectrum analyzer to BSA concentration has been developed. An economical and portable way of measuring salinity will help to study the shifts in the oceanic distribution of fresh and saline waters, which has been suggested to be linked with global warming. Cell protein concentration will aid in the study of nanomedicine. In addition, BSA concentration measurement will aid in investigating this model protein's cell culture and drug delivery applications. Tissue classification aids malignant tissue detection, and temperature sensor capability helps safeguard the system on chips. Integration of multiple laboratory operations onto a single chip like this with high sensitivity will save time and money for future research.

5.1 Future Work

With the advancements in plasmonics as an instrument for detecting and manipulating electromagnetic waves at subwavelength scales, numerous research avenues are opened that have the potential to impact a vast array of scientific and technological fields. Here are several possible future developments:

1. Future research may concentrate on the investigation of more advanced materials for the construction of plasmonic devices. The shortcomings of traditional metals underscore the need to consider alternative materials and models, and the problems associated with silver's oxidation necessitate the consideration of other metals with high chemical stability and enhanced biocompatibility. Furthermore, the plasmonic properties of alloys and doped substances could be investigated.

2. On the basis of the advancements in sensor design, such as the MIM refractive index sensor with rounded edges, additional design optimisations could be explored to improve sensitivity and specificity, reduce losses, and enhance electromagnetic wave confinement. These may include alternative geometries, proportions, and configurations of the sensor components.

3. While the use of plasmonic sensors in lab-on-a-chip technology has proven beneficial, there is still a great deal of opportunity for application diversification. Environmental monitoring, such as measuring air or water quality, is possible, as are medical applications such as disease detection and monitoring, which extend beyond to many

domains.

4. The integration of plasmonic devices with other optical, electronic, and mechanical systems could be investigated for the development of more complex functionalities. This could entail the development of hybrid systems that take advantage of the benefits of various technologies, such as the combination of plasmonic devices with photonic crystals or quantum systems.

5. Numerous studies could be conducted to enhance plasmonic device fabrication techniques. The incorporation of nanotechnology and cutting-edge manufacturing techniques, such as nanoscale 3D printing, could enable more complex and effective devices.

6. Future research may concentrate on developing and validating more precise computational models to predict the behaviour of plasmonic systems in light of the advances in computing power. This may entail incorporating more complex physics into the models, such as quantum effects or thermal influences.

References

[1] T. Birr, U. Zywietz, P. Chhantyal, B. N. Chichkov, and C. Reinhardt, "Ultrafast surface plasmon-polariton logic gates and half-adder," *Optics express*, vol. 23, no. 25, pp. 31 755–31 765, 2015.

[2] Y. Guo, L. Yan, W. Pan, B. Luo, K. Wen, Z. Guo, H. Li, and X. Luo, "A plasmonic splitter based on slot cavity," *Optics Express*, vol. 19, no. 15, pp. 13 831–13 838, 2011.

[3] Y. Chen, J. Dai, M. Yan, and M. Qiu, "Metal-insulator-metal plasmonic absorbers: influence of lattice," *Optics express*, vol. 22, no. 25, pp. 30 807–30 814, 2014.

[4] P. Neutens, L. Lagae, G. Borghs, and P. Van Dorpe, "Plasmon filters and resonators in metal-insulator-metal waveguides," *Optics Express*, vol. 20, no. 4, pp. 3408–3423, 2012.

[5] A. Akhavan, H. Ghafoorifard, S. Abdolhosseini, and H. Habibiyan, "Metal–insulator–metal waveguide-coupled asymmetric resonators for sensing and slow light applications," *IET Optoelectronics*, vol. 12, no. 5, pp. 220–227, 2018.

[6] M. A. A. Butt and N. Kazanskiy, "Enhancing the sensitivity of a standard plasmonic mim square ring resonator by incorporating the nano-dots in the cavity," *Photonics Letters of Poland*, vol. 12, no. 1, pp. 1–3, 2020.

[7] M. A. Butt, N. L. Kazanskiy, and S. N. Khonina, "Highly sensitive refractive index sensor based on plasmonic bow tie configuration," *Photonic sensors*, vol. 10, pp. 223–232, 2020.

[8] Z. Li, K. Wen, L. Chen, L. Lei, J. Zhou, D. Zhou, Y. Fang, and B. Wu, "Control of multiple fano resonances based on a subwavelength mim coupled cavities system," *IEEE access*, vol. 7, pp. 59 369–59 375, 2019.

[9] X. Li, D. Wang, S. Wang, L. Yuan, J. Lei, and X. Li, "Enhanced plasmonic-induced absorption using a cascade scheme and its application as refractive-index sensor," *Photonic Sensors*, vol. 10, pp. 162–170, 2020.

[10] B. Li, H. Sun, H. Zhang, Y. Li, J. Zang, X. Cao, X. Zhu, X. Zhao, and Z. Zhang, "Refractive index sensor based on the fano resonance in metal–insulator–metal waveguides coupled with a whistle-shaped cavity," *Micromachines*, vol. 13, no. 10, p. 1592, 2022.

[11] L. Liu, Z. Hu, M. Ye, Z. Yu, C. Ma, and J. Li, "On-chip refractive index sensor with ultra-high sensitivity based on sub-wavelength grating racetrack microring resonators and vernier effect," *IEEE Photonics Journal*, vol. 14, no. 5, pp. 1–7, 2022.

[12] Y. Qi, Y. Wang, X. Zhang, C. Liu, B. Hu, Y. Bai, and X. Wang, "A theoretical study of optically enhanced transmission characteristics of subwavelength metal y-shaped arrays and its application on refractive index sensor," *Results in Physics*, vol. 15, p. 102495, 2019.

[13] A. Rashed, B. Gudulluoglu, H. Yun, M. Habib, I. Boyaci, S. Hong, E. Ozbay, and H. Caglayan, "Highly-sensitive refractive index sensing by near-infrared metatronic nanocircuits," *ScieNtific REPORtS*, vol. 8, no. 1, p. 11457, 2018.

[14] X. Wang, J. Zhu, X. Wen, X. Wu, Y. Wu, Y. Su, H. Tong, Y. Qi, and H. Yang, "Wide range refractive index sensor based on a coupled structure of au nanocubes and au film," *Optical Materials Express*, vol. 9, no. 7, pp. 3079–3088, 2019.

[15] J. Yu, J. Zhu, S. Ye, and X. Wang, "Ultra-wide sensing range plasmonic refractive index sensor based on a two-dimensional circular-hole grating engraved on a gold film," *Results in Physics*, vol. 26, p. 104396, 2021.

[16] J. Zhu and N. Li, "Mim waveguide structure consisting of a semicircular resonant cavity coupled with a key-shaped resonant cavity," *Optics express*, vol. 28, no. 14, pp. 19 978–19 987, 2020.

[17] J. Chen, X. Lian, M. Zhao, and C. Xie, "Multimode fano resonances sensing based on a non-through mim waveguide with a square split-ring resonance cavity," *Biosensors*, vol. 12, no. 5, p. 306, 2022.

[18] X. Ren, K. Ren, and C. Ming, "Self-reference refractive index sensor based on independently controlled double resonances in side-coupled u-shaped resonators," *Sensors*, vol. 18, no. 5, p. 1376, 2018.

[19] T. Xu, Z. Geng, and Y. Su, "A potential plasmonic biosensor based asymmetric metal ring cavity with extremely narrow linewidth and high sensitivity," *Sensors*, vol. 21, no. 3, p. 752, 2021.

[20] X. Yang, E. Hua, M. Wang, Y. Wang, F. Wen, and S. Yan, "Fano resonance in a mim waveguide with two triangle stubs coupled with a split-ring nanocavity for sensing application," *Sensors*, vol. 19, no. 22, p. 4972, 2019.

[21] X. Zhang, S. Yan, J. Liu, Y. Ren, Y. Zhang, and L. Shen, "Refractive index sensor based on a metal-insulator-metal bus waveguide coupled with a u-shaped ring resonator," *Micromachines*, vol. 13, no. 5, p. 750, 2022.

[22] Z. Zhang, J. Yang, X. He, J. Zhang, J. Huang, D. Chen, and Y. Han, "Plasmonic refractive index sensor with high figure of merit based on concentric-rings resonator," *Sensors*, vol. 18, no. 1, p. 116, 2018.

[23] A. D. Rakić, A. B. Djurišić, J. M. Elazar, and M. L. Majewski, "Optical properties of metallic films for vertical-cavity optoelectronic devices," *Applied optics*, vol. 37, no. 22, pp. 5271–5283, 1998.

[24] M. C. Roco, M. C. Hersam, C. A. Mirkin, E. L. Hu, M. Brongersma, and A. Baca, "Applications: nanophotonics and plasmonics," *Nanotechnology Research Directions for Societal Needs in 2020: Retrospective and Outlook*, pp. 417–444, 2011.

[25] S. A. Maier and S. A. Maier, "Surface plasmon polaritons at metal/insulator interfaces," *Plasmonics: Fundamentals and Applications*, pp. 21–37, 2007.

[26] S. M. N. O. and S. Nelatury, *Elements of electromagnetics*. Oxford University Press, 2021.

[27] R. Al Mahmud, M. O. Faruque, and R. H. Sagor, "A highly sensitive plasmonic refractive index sensor based on triangular resonator," *Optics Communications*, vol. 483, p. 126634, 2021.

[28] S. A. Maier, "Plasmonics: The promise of highly integrated optical devices," *IEEE J. Sel. Top. Quantum Electron.*, vol. 12, no. 6, pp. 1671–1677, Nov. 2006.

[29] W. L. Barnes, A. Dereux, and T. W. Ebbesen, "Surface plasmon subwavelength optics," *nature*, vol. 424, no. 6950, pp. 824–830, 2003.

[30] B. Luff, R. Harris, J. Wilkinson, R. Wilson, and D. Schiffrin, "Integrated-optical directional coupler biosensor," *Optics Letters*, vol. 21, no. 8, pp. 618–620, 1996.

[31] J. Park, H. Kim, and B. Lee, "High order plasmonic bragg reflection in the metal-insulator-metal waveguide bragg grating," *Optics express*, vol. 16, no. 1, pp. 413–425, 2008.

[32] M. Akhlaghi and M. Kaboli, "Investigating the optical xnor gate using plasmonic nano-rods," *Photonics and Nanostructures-Fundamentals and Applications*, vol. 19, pp. 24–30, 2016.

[33] Y.-Y. Xie, C. He, J.-C. Li, T.-T. Song, Z.-D. Zhang, and Q.-R. Mao, "Theoretical investigation of a plasmonic demultiplexer in mim waveguide crossing with multiple side-coupled hexagonal resonators," *IEEE Photonics Journal*, vol. 8, no. 5, pp. 1–12, 2016.

[34] X.-P. Jin, X.-G. Huang, J. Tao, X.-S. Lin, and Q. Zhang, "A novel nanometeric plasmonic refractive index sensor," *IEEE transactions on nanotechnology*, vol. 9, no. 2, pp. 134–137, 2010.

[35] R. H. Sagor, M. F. Hassan, S. Sharmin, T. Z. Adry, and M. A. R. Emon, "Numerical investigation of an optimized plasmonic on-chip refractive index sensor for temperature and blood group detection," *Results in Physics*, vol. 19, p. 103611, 2020.

[36] M. Butt, S. Khonina, and N. Kazanskiy, "Plasmonic refractive index sensor based on metal–insulator-metal waveguides with high sensitivity," *Journal of Modern Optics*, vol. 66, no. 9, pp. 1038–1043, 2019.

[37] Y. Binfeng, H. Guohua, Z. Ruohu, and C. Yiping, "Design of a compact and high sensitive refractive index sensor base on metal-insulator-metal plasmonic bragg grating," *Optics Express*, vol. 22, no. 23, pp. 28 662–28 670, 2014.

[38] M. Pi, H. Zhao, C. Li, Y. Min, Z. Peng, J. Ji, Y. Huang, F. Song, L. Liang, Y. Zhang *et al.*, "Mid-infrared chalcogenide slot waveguide plasmonic resonator sensor embedded with au nanorods for surface-enhanced infrared absorption spectroscopy," *Results in Physics*, vol. 42, p. 106005, 2022.

[39] H. Sahoo, "Fluorescent labeling techniques in biomolecules: a flashback," *RSC advances*, vol. 2, no. 18, pp. 7017–7029, 2012.

[40] S. Khani, M. Danaie, and P. Rezaei, "Realization of single-mode plasmonic bandpass filters using improved nanodisk resonators," *Optics Communications*, vol. 420, pp. 147–156, 2018.

[41] R. Malureanu and A. Lavrinenko, "Ultra-thin films for plasmonics: a technology overview," *Nanotechnology Reviews*, vol. 4, no. 3, pp. 259–275, 2015.

[42] H. H. Goldstine and A. Goldstine, "The electronic numerical integrator and computer (eniac)," in *The Origins of Digital Computers: Selected Papers*. Springer, 1946, pp. 359–373.

[43] T. Haigh, P. Priestley, and C. Rope, *ENIAC in Action: Making and Remaking the Modern Computer*, ser. History of Computing. MIT Press, 2016. [Online]. Available: https://books.google.com.bd/books?id=_oqBCwAAQBAJ

[44] D. A. B. Miller and H. M. Ozaktas, "Limit to the bit-rate capacity of electrical interconnects from the aspect ratio of the system architecture," *Journal of parallel and distributed computing*, vol. 41, no. 1, pp. 42–52, 1997.

[45] S. Esener, "Implementation and prospects for chip-to-chip free-space optical interconnects," in *International Electron Devices Meeting. Technical Digest (Cat. No.01CH37224)*, 2001, pp. 23.5.1–23.5.4.

[46] D. N. Batchelder and J. P. Willson, "Optical surface plasmon sensor device," Jul. 4 1989, uS Patent 4,844,613.

[47] R. Garabedian, C. Gonzalez, J. Richards, A. Knoesen, R. Spencer, S. Collins, and R. Smith, "Microfabricated surface plasmon sensing system," *Sensors and Actuators A: Physical*, vol. 43, no. 1-3, pp. 202–207, 1994.

[48] S. Nelson, K. S. Johnston, and S. S. Yee, "High sensitivity surface plasmon resonace sensor based on phase detection," *Sensors and actuators B: Chemical*, vol. 35, no. 1-3, pp. 187–191, 1996.

[49] J. Homola, J. Čtyrokỳ, M. Skalskỳ, J. Hradilova, and P. Kolářová, "A surface plasmon resonance based integrated optical sensor," *Sensors and Actuators B: Chemical*, vol. 39, no. 1-3, pp. 286–290, 1997.

[50] M. W. Foster, "Surface plasmon resonance sensor and methods for the utilization thereof," Jan. 16 1996, uS Patent 5,485,277.

[51] J. Čtyrokỳ, J. Homola, P. Lambeck, S. Musa, H. Hoekstra, R. Harris, J. Wilkinson, B. Usievich, and N. Lyndin, "Theory and modelling of optical waveguide sensors utilising surface plasmon resonance," *Sensors and Actuators B: Chemical*, vol. 54, no. 1-2, pp. 66–73, 1999.

[52] J. J. Mock, D. R. Smith, and S. Schultz, "Local refractive index dependence of plasmon resonance spectra from individual nanoparticles," *Nano letters*, vol. 3, no. 4, pp. 485–491, 2003.

[53] E. M. Larsson, J. Alegret, M. Käll, and D. S. Sutherland, "Sensing characteristics of nir localized surface plasmon resonances in gold nanorings for application as ultrasensitive biosensors," *Nano letters*, vol. 7, no. 5, pp. 1256–1263, 2007.

[54] A. G. Brolo, R. Gordon, B. Leathem, and K. L. Kavanagh, "Surface plasmon sensor based on the enhanced light transmission through arrays of nanoholes in gold films," *Langmuir*, vol. 20, no. 12, pp. 4813–4815, 2004.

[55] A. Lesuffleur, H. Im, N. C. Lindquist, and S.-H. Oh, "Periodic nanohole arrays with shape-enhanced plasmon resonance as real-time biosensors," *Applied Physics Letters*, vol. 90, no. 24, 2007.

[56] E. J. R. Vesseur, R. De Waele, H. Lezec, H. Atwater, F. J. García de Abajo, and A. Polman, "Surface plasmon polariton modes in a single-crystal au nanoresonator fabricated using focused-ion-beam milling," *Applied Physics Letters*, vol. 92, no. 8, 2008.

[57] Y. Fang and M. Sun, "Nanoplasmonic waveguides: towards applications in integrated nanophotonic circuits," *Light: Science & Applications*, vol. 4, no. 6, pp. e294–e294, 2015.

[58] P. Saeidi, B. Jakoby, G. Pühringer, A. Tortschanoff, G. Stocker, F. Dubois, J. Spettel, T. Grille, and R. Jannesari, "Designing mid-infrared gold-based plasmonic slot waveguides for co2-sensing applications," *Sensors*, vol. 21, no. 8, p. 2669, 2021.

[59] J. Becker, A. Trügler, A. Jakab, U. Hohenester, and C. Sönnichsen, "The optimal aspect ratio of gold nanorods for plasmonic bio-sensing," *Plasmonics*, vol. 5, pp. 161–167, 2010.

[60] Y.-F. C. Chau, "Enhanced plasmonic waveguide sensing performance with a semicircular-ring resonator," *Micro and Nanostructures*, vol. 174, p. 207469, 2023.

[61] Y.-F. Chou Chau, "Multiple-mode bowtie cavities for refractive index and glucose sensors working in visible and near-infrared wavelength ranges," *Plasmonics*, vol. 16, no. 5, pp. 1633–1644, 2021.

[62] Y.-F. C. Chau, "Mid-infrared sensing properties of a plasmonic metal–insulator–metal waveguide with a single stub including defects," *Journal of Physics D: Applied Physics*, vol. 53, no. 11, p. 115401, 2020.

[63] K. S. Rashid, I. Tathfif, A. A. Yaseer, M. F. Hassan, and R. H. Sagor, "Cog-shaped refractive index sensor embedded with gold nanorods for temperature sensing of multiple analytes," *Optics Express*, vol. 29, no. 23, pp. 37 541–37 554, 2021.

[64] I. Tathfif, K. S. Rashid, A. A. Yaseer, and R. H. Sagor, "Alternative material titanium nitride based refractive index sensor embedded with defects: An emerging solution in sensing arena," *Results in Physics*, vol. 29, p. 104795, 2021.

[65] M. A. Butt, "Numerical assessment of a metal-insulator-metal waveguide-based plasmonic sensor system for the recognition of tuberculosis in blood plasma," *Micromachines*, vol. 14, no. 4, p. 729, 2023.

[66] G. Raschke, S. Kowarik, T. Franzl, C. Sönnichsen, T. Klar, J. Feldmann, A. Nichtl, and K. Kürzinger, "Biomolecular recognition based on single gold nanoparticle light scattering," *Nano letters*, vol. 3, no. 7, pp. 935–938, 2003.

[67] A. D. McFarland and R. P. Van Duyne, "Single silver nanoparticles as real-time optical sensors with zeptomole sensitivity," *Nano letters*, vol. 3, no. 8, pp. 1057–1062, 2003.

[68] C. L. Baciu, J. Becker, A. Janshoff, and C. Sonnichsen, "Protein–membrane interaction probed by single plasmonic nanoparticles," *Nano Letters*, vol. 8, no. 6, pp. 1724–1728, 2008.

[69] K.-S. Lee and M. A. El-Sayed, "Gold and silver nanoparticles in sensing and imaging: sensitivity of plasmon response to size, shape, and metal composition," *The Journal of Physical Chemistry B*, vol. 110, no. 39, pp. 19 220–19 225, 2006.

[70] Y. Khalavka, J. Becker, and C. Sonnichsen, "Synthesis of rod-shaped gold nanorattles with improved plasmon sensitivity and catalytic activity," *Journal of the American Chemical Society*, vol. 131, no. 5, pp. 1871–1875, 2009.

[71] N. Liu, T. Weiss, M. Mesch, L. Langguth, U. Eigenthaler, M. Hirscher, C. Sonnichsen, and H. Giessen, "Planar metamaterial analogue of electromagnetically induced transparency for plasmonic sensing," *Nano letters*, vol. 10, no. 4, pp. 1103–1107, 2010.

[72] J. Becker, I. Zins, A. Jakab, Y. Khalavka, O. Schubert, and C. Sönnichsen, "Plasmonic focusing reduces ensemble linewidth of silver-coated gold nanorods," *Nano letters*, vol. 8, no. 6, pp. 1719–1723, 2008.

[73] Y. Tang, Z. Zhang, R. Wang, Z. Hai, C. Xue, W. Zhang, and S. Yan, "Refractive index sensor based on fano resonances in metal-insulator-metal waveguides coupled with resonators," *Sensors*, vol. 17, no. 4, p. 784, 2017.

[74] X. Zhang, Y. Qi, P. Zhou, H. Gong, B. Hu, and C. Yan, "Refractive index sensor based on fano resonances in plasmonic waveguide with dual side-coupled ring resonators," *Photonic sensors*, vol. 8, pp. 367–374, 2018.

[75] M. F. Hassan, M. M. Hasan, M. Radoan, and R. H. Sagor, "Design and performance analysis of an ultra-compact nano-plasmonic refractive index sensor," in *2020 8th International Electrical Engineering Congress (iEECON)*. IEEE, 2020, pp. 1–5.

[76] Y. Chowdhury, "Plasmonic waveguides: design and comparative study," 2011.

[77] Y.-F. Chou Chau, T. Y. Ming, C.-T. Chou Chao, R. Thotagamuge, M. R. R. Kooh, H. J. Huang, C. M. Lim, and H.-P. Chiang, "Significantly enhanced coupling effect and gap plasmon resonance in a mim-cavity based sensing structure," *Scientific Reports*, vol. 11, no. 1, p. 18515, 2021.

[78] S. E. El-Zohary, A. Azzazi, H. Okamoto, T. Okamoto, M. Haraguchi, and M. A. Swillam, "Resonance-based integrated plasmonic nanosensor for lab-on-chip applications," *Journal of Nanophotonics*, vol. 7, no. 1, pp. 073 077–073 077, 2013.

[79] A. Rakib, A. T. B. Siddique, M. S. Sakib, M. O. Faruque, and R. H. Sagor, "A numerical analysis of a highly sensitive hexagonal plasmonic refractive index sensor," *Optics Communications*, vol. 530, p. 129205, 2023.

[80] J. Zhang, X. Wang, J. Zhu, T. Chen, L. Zhang, H. Yang, C. Tang, Y. Qi, and J. Yu, "Metal–insulator–metal waveguide structure coupled with t-type and ring resonators for independent and tunable multiple fano resonance and refractive index sensing," *Optics Communications*, vol. 528, p. 128993, 2023.

[81] S. Khani and M. Afsahi, "Optical refractive index sensors based on plasmon-induced transparency phenomenon in a plasmonic waveguide coupled to stub and nano-disk resonators," *Plasmonics*, vol. 18, no. 1, pp. 255–270, 2023.

[82] H. Guo, Z. Chen, J. Qi, M. Jiang, J. Chen, Y. Li, and Q. Sun, "Ultra-high figure of merit refractive index sensor based on concentric ring and disk resonator," *Journal of Optics*, vol. 52, no. 1, pp. 120–127, 2023.

[83] H. Bensalah, A. Hocini, H. Bahri, D. Khedrouche, S. Ingebrandt, and V. Pachauri, "A plasmonic refractive index sensor with high sensitivity and its application for temperature and detection of biomolecules," *Journal of Optics*, pp. 1–12, 2022.

[84] S. Rohimah, H. Tian, J. Wang, J. Chen, J. Li, X. Liu, J. Cui, Q. Xu, and Y. Hao, "Fano resonance in the plasmonic structure of mim waveguide with r-shaped resonator for refractive index sensor," *Plasmonics*, vol. 17, no. 4, pp. 1681–1689, 2022.

[85] S. Tavana and S. Bahadori-Haghighi, "Visible-range double fano resonance metal–insulator-metal plasmonic waveguide for optical refractive index sensing," *Plasmonics*, vol. 17, no. 6, pp. 2441–2449, 2022.

[86] V. Najjari, S. Mirzanejhad, and A. Ghadi, "Plasmonic refractive index sensor and plasmonic bandpass filter including graded 4-step waveguide based on fano resonances," *Plasmonics*, vol. 17, no. 4, pp. 1809–1817, 2022.

[87] N. Saha, G. Brunetti, A. Kumar, M. N. Armenise, and C. Ciminelli, "Highly sensitive refractive index sensor based on polymer bragg grating: A case study on extracellular vesicles detection," *Biosensors*, vol. 12, no. 6, p. 415, 2022.

[88] Q. Shangguan, Y. Zhao, Z. Song, J. Wang, H. Yang, J. Chen, C. Liu, S. Cheng, W. Yang, and Z. Yi, "High sensitivity active adjustable graphene absorber for refractive index sensing applications," *Diamond and Related Materials*, vol. 128, p. 109273, 2022.

[89] S. K. Patel, N. Solanki, S. Charola, J. Parmar, R. Zakaria, O. S. Faragallah, M. M. Eid, and A. N. Z. Rashed, "Graphene based highly sensitive refractive index sensor using double split ring resonator metasurface," *Optical and Quantum Electronics*, vol. 54, no. 3, p. 203, 2022.

[90] R. H. Sagor, M. F. Hassan, A. A. Yaseer, E. Surid, and M. I. Ahmed, "Highly sensitive refractive index sensor optimized for blood group sensing utilizing the fano resonance," *Applied Nanoscience*, vol. 11, pp. 521–534, 2021.

[91] R. Al Mahmud, M. O. Faruque, and R. H. Sagor, "Plasmonic refractive index sensor based on ring-type pentagonal resonator with high sensitivity," *Plasmonics*, vol. 16, pp. 873–880, 2021.

[92] X. Wang, J. Zhu, Y. Xu, Y. Qi, L. Zhang, H. Yang, and Z. Yi, "A novel plasmonic refractive index sensor based on gold/silicon complementary grating structure," *Chinese Physics B*, vol. 30, no. 2, p. 024207, 2021.

[93] J. Zhu and C. Wu, "Optical refractive index sensor with fano resonance based on original mim waveguide structure," *Results in Physics*, vol. 21, p. 103858, 2021.

[94] S. Khani and M. Hayati, "An ultra-high sensitive plasmonic refractive index sensor using an elliptical resonator and mim waveguide," *Superlattices and Microstructures*, vol. 156, p. 106970, 2021.

[95] S. Asgari, S. Pooretemad, and N. Granpayeh, "Plasmonic refractive index sensor based on a double concentric square ring resonator and stubs," *Photonics and Nanostructures-Fundamentals and Applications*, vol. 42, p. 100857, 2020.

[96] Y. Fang, K. Wen, Z. Li, B. Wu, and Z. Guo, "Plasmonic refractive index sensor with multi-channel fano resonances based on mim waveguides," *Modern Physics Letters B*, vol. 34, no. 16, p. 2050173, 2020.

[97] N. Amoosoltani, N. Yasrebi, A. Farmani, and A. Zarifkar, "A plasmonic nanobiosensor based on two consecutive disk resonators and unidirectional reflectionless propagation effect," *IEEE Sensors Journal*, vol. 20, no. 16, pp. 9097–9104, 2020.

[98] M. Butt, S. Khonina, and N. Kazanskiy, "An array of nano-dots loaded mim square ring resonator with enhanced sensitivity at nir wavelength range," *Optik*, vol. 202, p. 163655, 2020.

[99] A. Alipour, A. Mir, and A. Farmani, "Ultra high-sensitivity and tunable dual-band perfect absorber as a plasmonic sensor," *Optics & Laser Technology*, vol. 127, p. 106201, 2020.

[100] R. El Haffar, A. Farkhsi, and O. Mahboub, "Optical properties of mim plasmonic waveguide with an elliptical cavity resonator," *Applied Physics A*, vol. 126, pp. 1–10, 2020.

[101] M. Bazgir, M. Jalalpour, F. B. Zarrabi, and A. S. Arezoomand, "Design of an optical switch and sensor based on a mim coupled waveguide using a dna composite," *Journal of Electronic Materials*, vol. 49, pp. 2173–2178, 2020.

[102] G. Qiu, Z. Gai, Y. Tao, J. Schmitt, G. A. Kullak-Ublick, and J. Wang, "Dual-functional plasmonic photothermal biosensors for highly accurate severe acute respiratory syndrome coronavirus 2 detection," *ACS nano*, vol. 14, no. 5, pp. 5268–5277, 2020.

[103] Y. Zhang, Y. Kuang, Z. Zhang, Y. Tang, J. Han, R. Wang, J. Cui, Y. Hou, and W. Liu, "High-sensitivity refractive index sensors based on fano resonance in the plasmonic system of splitting ring cavity-coupled mim waveguide with tooth cavity," *Applied Physics A*, vol. 125, pp. 1–5, 2019.

[104] Y. Wen, Y. Sun, C. Deng, L. Huang, G. Hu, B. Yun, R. Zhang, and Y. Cui, "High sensitivity and fom refractive index sensing based on fano resonance in all-grating racetrack resonators," *Optics Communications*, vol. 446, pp. 141–146, 2019.

[105] S. Asgari and N. Granpayeh, "Tunable mid-infrared refractive index sensor composed of asymmetric double graphene layers," *IEEE sensors Journal*, vol. 19, no. 14, pp. 5686–5691, 2019.

[106] R. Zafar, S. Nawaz, G. Singh, A. d'Alessandro, and M. Salim, "Plasmonics-based refractive index sensor for detection of hemoglobin concentration," *IEEE Sensors Journal*, vol. 18, no. 11, pp. 4372–4377, 2018.

[107] M. J. Al Mahmod, R. Hyder, and M. Z. Islam, "A highly sensitive metal–insulator–metal ring resonator-based nanophotonic structure for biosensing applications," *IEEE Sensors Journal*, vol. 18, no. 16, pp. 6563–6568, 2018.

[108] X. Yi, J. Tian, and R. Yang, "Tunable fano resonance in plasmonic mdm waveguide with a square type split-ring resonator," *Optik*, vol. 171, pp. 139–148, 2018.

[109] S. Ghorbani, M. A. Dashti, and M. Jabbari, "Plasmonic nano-sensor based on metal-dielectric-metal waveguide with the octagonal cavity ring," *Laser Physics*, vol. 28, no. 6, p. 066208, 2018.

[110] M. F. Hassan, R. H. Sagor, M. R. Amin, M. R. Islam, and M. S. Alam, "Point of care detection of blood electrolytes and glucose utilizing nano-dot enhanced plasmonic biosensor," *IEEE Sensors Journal*, vol. 21, no. 16, pp. 17 749–17 757, 2021.

[111] S. A. Maier, "Plasmonics: The promise of highly integrated optical devices," *IEEE Journal of selected topics in Quantum Electronics*, vol. 12, no. 6, pp. 1671–1677, 2006.

[112] H. Raether, "Surface plasmons on smooth surfaces," *Surface plasmons on smooth and rough surfaces and on gratings*, pp. 4–39, 2006.

[113] L. Yang, P. Li, H. Wang, and Z. Li, "Surface plasmon polariton waveguides with subwavelength confinement," *Chinese Physics B*, vol. 27, no. 9, p. 094216, 2018.

[114] D. G. Rabus, C. Sada, D. G. Rabus, and C. Sada, "Ring resonators: Theory and modeling," *Integrated Ring Resonators: A Compendium*, pp. 3–46, 2020.

[115] C. Wu, H. Ding, T. Huang, X. Wu, B. Chen, K. Ren, and S. Fu, "Plasmon-induced transparency and refractive index sensing in side-coupled stub-hexagon resonators," *Plasmonics*, vol. 13, pp. 251–257, 2018.

[116] J.-M. Jin, *The finite element method in electromagnetics*. John Wiley & Sons, 2015.

[117] N. Kazanskiy, M. Butt, and S. Khonina, "Nanodots decorated mim semi-ring resonator cavity for biochemical sensing applications," *Photonics and Nanostructures-Fundamentals and Applications*, vol. 42, p. 100836, 2020.

[118] D. G. Rabus, *Integrated ring resonators*. Springer, 2007.

[119] S. Arscott and D. Troadec, "Electrospraying from nanofluidic capillary slot," *Applied Physics Letters*, vol. 87, no. 13, p. 134101, 2005.

[120] A. Vorobyev and C. Guo, "Metal pumps liquid uphill," *Applied Physics Letters*, vol. 94, no. 22, p. 224102, 2009.

[121] A. Boltasseva, "Plasmonic components fabrication via nanoimprint," *Journal of Optics A: Pure and Applied Optics*, vol. 11, no. 11, p. 114001, 2009.

[122] S. Y. Chou and P. R. Krauss, "Imprint lithography with sub-10 nm feature size and high throughput," *Microelectronic Engineering*, vol. 35, no. 1-4, pp. 237–240, 1997.

[123] U. Plachetka, M. Bender, A. Fuchs, B. Vratzov, T. Glinsner, F. Lindner, and H. Kurz, "Wafer scale patterning by soft uv-nanoimprint lithography," *Microelectronic Engineering*, vol. 73, pp. 167–171, 2004.

[124] F. Hamouda, G. Barbillon, F. Gaucher, and B. Bartenlian, "Sub-200 nm gap electrodes by soft uv nanoimprint lithography using polydimethylsiloxane mold without external pressure," *Journal of Vacuum Science & Technology B, Nanotechnology and Microelectronics: Materials, Processing, Measurement, and Phenomena*, vol. 28, no. 1, pp. 82–85, 2010.

[125] S.-W. Lee, K.-S. Lee, J. Ahn, J.-J. Lee, M.-G. Kim, and Y.-B. Shin, "Highly sensitive biosensing using arrays of plasmonic au nanodisks realized by nanoimprint lithography," *ACS nano*, vol. 5, no. 2, pp. 897–904, 2011.

[126] M. Danaie and A. Shahzadi, "Design of a high-resolution metal–insulator–metal plasmonic refractive index sensor based on a ring-shaped si resonator," *Plasmonics*, vol. 14, no. 6, pp. 1453–1465, 2019.

[127] S. Kamada, T. Okamoto, S. E. El-Zohary, and M. Haraguchi, "Design optimization and fabrication of mach-zehnder interferometer based on mim plasmonic waveguides," *Optics Express*, vol. 24, no. 15, pp. 16 224–16 231, 2016.

[128] F. Stade, A. Heeren, M. Fleischer, and D. Kern, "Fabrication of metallic nanostructures for investigating plasmon-induced field enhancement," *Microelectronic engineering*, vol. 84, no. 5-8, pp. 1589–1592, 2007.

[129] A. Campos, A. Arbouet, J. Martin, D. Gerard, J. Proust, J. Plain, and M. Kociak, "Plasmonic breathing and edge modes in aluminum nanotriangles," *Acs Photonics*, vol. 4, no. 5, pp. 1257–1263, 2017.

[130] R. Curry, B. Dickson, and I. Yashayaev, "A change in the freshwater balance of the atlantic ocean over the past four decades," *Nature*, vol. 426, no. 6968, pp. 826–829, 2003.

[131] X. Quan and E. S. Fry, "Empirical equation for the index of refraction of seawater," *Applied optics*, vol. 34, no. 18, pp. 3477–3480, 1995.

[132] G. C. Brown, "Total cell protein concentration as an evolutionary constraint on the metabolic control distribution in cells," *Journal of theoretical biology*, vol. 153, no. 2, pp. 195–203, 1991.

[133] E. Alessio, R. S. Bonadio, L. Buson, F. Chemello, and S. Cagnin, "A single cell but many different transcripts: a journey into the world of long non-coding rnas," *International journal of molecular sciences*, vol. 21, no. 1, p. 302, 2020.

[134] R. Barer and S. Joseph, "Refractometry of living cells: Part i. basic principles," *Journal of Cell Science*, vol. 3, no. 32, pp. 399–423, 1954.

[135] A. Jahanban-Esfahlan, A. Ostadrahimi, R. Jahanban-Esfahlan, L. Roufegarinejad, M. Tabibiazar, and R. Amarowicz, "Recent developments in the detection of bovine serum albumin," *International journal of biological macromolecules*, vol. 138, pp. 602–617, 2019.

[136] G. L. Francis, "Albumin and mammalian cell culture: implications for biotechnology applications," *Cytotechnology*, vol. 62, no. 1, pp. 1–16, 2010.

[137] A. C. H and A. Ravindran, "Bsa nanoparticle loaded atorvastatin calcium-a new facet for an old drug," *PloS one*, vol. 9, no. 2, p. e86317, 2014.

[138] M. M. Pereira, S. N. Pedro, M. V. Quental, Á. S. Lima, J. A. Coutinho, and M. G. Freire, "Enhanced extraction of bovine serum albumin with aqueous biphasic systems of phosphonium-and ammonium-based ionic liquids," *Journal of biotechnology*, vol. 206, pp. 17–25, 2015.

[139] C.-Y. Tan and Y.-X. Huang, "Dependence of refractive index on concentration and temperature in electrolyte solution, polar solution, nonpolar solution, and protein solution," *Journal of Chemical & Engineering Data*, vol. 60, no. 10, pp. 2827–2833, 2015.

[140] H. Liu, H. Li, Q. Wang, M. Wang, Y. Ding, C. Zhu, and D. Cheng, "Temperature-compensated magnetic field sensor based on surface plasmon resonance and directional resonance coupling in a d-shaped photonic crystal fiber," *Optik*, vol. 158, pp. 1402–1409, 2018.

[141] M. Matiatou, P. Giannios, S. Koutsoumpos, K. G. Toutouzas, G. C. Zografos, and K. Moutzouris, "Data on the refractive index of freshly-excised human tissues in the visible and near-infrared spectral range," *Results in Physics*, vol. 22, p. 103833, 2021.

[142] M. Rahmatiyar, M. Afsahi, and M. Danaie, "Design of a refractive index plasmonic sensor based on a ring resonator coupled to a mim waveguide containing tapered defects," *Plasmonics*, vol. 15, pp. 2169–2176, 2020.

[143] M. A. Butt, A. Kaźmierczak, N. L. Kazanskiy, and S. N. Khonina, "Metal-insulator-metal waveguide-based racetrack integrated circular cavity for refractive index sensing application," *Electronics*, vol. 10, no. 12, p. 1419, 2021.

[144] Y.-F. Chou Chau, C.-T. Chou Chao, H. J. Huang, M. R. R. Kooh, N. T. R. N. Kumara, C. M. Lim, and H.-P. Chiang, "Ultrawide bandgap and high sensitivity of a

plasmonic metal-insulator-metal waveguide filter with cavity and baffles," *Nanomaterials*, vol. 10, no. 10, p. 2030, 2020.

[145] M. R. Rakhshani and M. A. Mansouri-Birjandi, "Engineering hexagonal array of nanoholes for high sensitivity biosensor and application for human blood group detection," *IEEE Transactions on Nanotechnology*, vol. 17, no. 3, pp. 475–481, 2018.

[146] Y. M. Tan, C.-T. C. Chao, M. R. R. Kooh, H. J. Huang, R. Thotagamuge, C. M. Lim, H.-P. Chiang, and Y.-F. C. Chau, "Mid infrared sensing structure based on a metal–insulator–metal waveguides with a triangular-shaped resonator," *Optics Communications*, vol. 516, p. 128282, 2022.